Electroaerodynamic characteristics of a needle-to-ring positive corona discharge: self-consistent modeling and turbulence effects

Tuan Dung Nguyen, François Rogier, Konstantinos Kourtzanidis

Electroaerodynamic characteristics of a needle-to-ring positive corona discharge: self-consistent modeling and turbulence effects

Nguyen Tuan Dung[1,2,4], François Rogier[2] and Konstantinos Kourtzanidis[3,*]

[1] Institut de Mathématiques de Toulouse, CNRS UMR 5219, Université Paul Sabatier, 118 Route de Narbonne, 31062 Toulouse Cedex 9

[2] The French Aerospace Lab (ONERA), 2 avenue Edouard Belin, 31055 Toulouse Cedex 4

[3] Chemical Process & Energy Resources Institute (CPERI), Centre for Research & Technology Hellas (CERTH), 6th km Charilaou-Thermi, Thermi, 57001 Thessaloniki, Greece

[4] *Current address:* Laboratoire de Mécanique, Modélisation & Procédés Propres, CNRS UMR 7340, Université d'Aix-Marseille, 38 rue Joliot-Curie, 13451 Marseille Cedex 20

[*] corresponding author

E-mail: kourtzanidis@certh.gr

Abstract. We report on the voltage-current characteristics as well as the voltage-velocity characteristics of a needle-to-ring configuration by self-consistent, 2D-axisymmetric, multi-physics plasma-fluid simulations. Parametric studies are performed to investigate the effects of background ionization level on the plasma electrical characteristics as well as turbulence parameters on the resulting flow. Our results show that the discharge and the flow exhibit an annular structure around the needle (anode) tip, with a maximum positive ion density from 1.5×10^{18}-2.7×10^{18} m^{-3} and a maximum flow velocity from 10-15 m s^{-1}, for overvoltages between 4-12 kV and an anode-cathode distance of 20 mm. Good overall agreement with experimental findings is achieved, noting that background ionization level can be used as a tuning parameter to better match experimentally measured current values even with a simplified plasma-chemistry. A better agreement between simulation and experiments is achieved concerning the voltage-velocity curves. Therefore, the latter are likely to be better indicators for assessing and validating electroaerodynamic effects of corona actuators through numerical modeling. The flow dynamics indicate that positive-corona-induced ionic winds are most likely laminar to turbulent transitional flows, with a ratio between eddy viscosity and air viscosity varying between 0-200.

Keywords: positive corona discharge, needle-to-ring actuator, plasma simulation, ionic wind, electroaerodynamic, electron floor density, RANS turbulence model

1. Introduction

Atmospheric-pressure, corona discharges in air are well-known to produce electroaerodynamic (EAD, also called electrohydronamic) force due to charged-neutral species collisions and momentum transfer to the latter. The consequence of this momentum exchange is the generation of a gas flow, typically called ionic wind. This purely electrical mechanism of momentum addition to the background gas has been leveraged in various applications ranging from electrostatic precipitators [1, 2], heat dissipation/cooling of electronic components [3, 4, 5], fanless blowers/pumps [6, 7], water harvesting [8], aerodynamic flow control [9] to solid-state propulsion. Focusing on the latter, and since the 2009 NASA technical report [10] which concluded that corona/EAD-based systems are not very practical for in-atmosphere propulsion, several authors [11, 12, 13, 14, 15, 16] have continued investigating EAD propulsion while working on improved configurations as well as engineering aspects towards the demonstration of a solid-state, all-electric, EAD-propelled airplane. Such demonstration has been achieved in 2018 by MIT researchers [17], achieving a continuous steady-level flight of a five-meter wingspan, fixed-wing airplane - a proof of concept for EAD propulsion. Since then, the field has gained significant momentum with main efforts focused on improved thrust generation and reduced power consumption [18, 19]. Next generation ultra-lightweight and high power density batteries [20] and lightweight HV generators [21] can foster the applicability and realization of EAD propulsion systems in the near future.

In the pursuit of cost efficient (in terms of CPU time) numerical models, which can aid the design, parametrization and optimization of EAD systems, two main approaches can be found in the literature, (i) unipolar models based on the division of the computational domain into an ionization zone and a drift zone, and (ii) self-consistent, multi-species simulations.

In the unipolar approach, inside the drift zone, only the ion drift-diffusion equation is solved with either unsteady (time-dependent) or steady-state solvers. The electric field is given by the solution of Poisson equation in the drift zone. The ionization zone (typically small and comparable to the curvature radius of the active electrode) is not resolved: as such, there is a need for simplified approximations on the electric field distribution at the electrode. Typically this is determined using Deutsch or Kaptzov approximations, where the electric field at the electrode is assumed constant and uniform after the onset of the corona discharge, and set to Peek's onset criterion. The space charge density (or ion flux or charge injection) is thus gradually increased (or decreased) in the computation domain until the electric field at the ionization zone boundary (often coinciding with the electrode surface) equals the critical value defined by Peek. Different approximations, based on the so-called direct ionization criterion [22] or other charge injection laws [23] have also been proposed to determine the constant corona electric field criterion at the electrode for arbitrary electrode shape. The benefits of such approach are straightforward: the computationally demanding ionization zone (owed to both necessary spatial discretization refinement and temporal timestep restrictions) is not resolved and thus fast

computations are possible. Nevertheless, all variations of this approach, and despite the calculated, overall-satisfying V-I characteristics, deviate significantly from each other [24] especially for high applied voltages (high discharge currents) and short gap distances, while the input/tuning parameters used (e.g. experimentally measured anode current as in Ref. [25]) render these approaches impractical for the design and optimization of novel configurations without the need (and related cost) of experimentation.

Self-consistent simulations, on the other hand, rely on resolution of plasma dynamics in all gas zones, whether they are near-electrode ionization regions or interelectrode region, with a set of boundary conditions derived from physical interactions with solid walls. Hydrodynamic (fluid) descriptions are widely used in simulation of gas discharges, and because of the low-temperature, high gas density nature of the atmospheric air plasmas (relevant to EAD atmospheric propulsion), collisionality prevails and the drift velocity of charges is directly computed from the electric field via explicit mobility laws, instead of from momentum conservation laws (as e.g. in Navier-Stokes equations). As a result, drift-diffusion discharge models consist of mass conservation laws in a convection-diffusion-reaction form, coupled with an electric potential equation (for example, see section 2.1). Different applications of self-consistent hydrodynamic models can be found in [26, 27, 28, 29] (for corona discharges) or [30, 31, 32, 33, 34, 35, 36, 37] (DBD discharges), etc. The immediate advantage of self-consistent approach is its capability to capture correctly the plasma dynamics in all gas zones (including near-electrode ones), which are utmost important to self-consistently describe the discharge nature or the mechanism of EAD propulsion without pre-defined tuning. However, the need to discretize the computationally demanding ionization zones, as mentioned before, is the main drawback of this approach. Indeed, the characteristic timescale of electron drift inside a sheath is on the order of picoseconds but for ionic wind, it is milliseconds, which usually lead to extensive CPU time, especially if explicit time schemes are employed. For instance, a steady-state wire-to-wire corona discharge simulation with the explicit formulation of ONERA's multi-species, multi-reactions plasma solver COPAIER [38] (using the Runge-Kutta-Heun time-integration scheme), can take up to a couple of weeks on multiple processors to finish.

In addition, both approaches, unipolar and self-consistent, suffer from multiple uncertainties, most of them are typical for plasma models which are subject to various tuning parameters: chemistry sets (kinetic schemes), rate and transport coefficients, photoionization and/or initial/floor values of charged species density, secondary electron emission coefficient, etc. And furthermore, the additional but necessary coupling of discharge models with CFD models to capture the ionic wind dynamics, introduces additional uncertainties, manifesting mostly in terms of turbulence and related turbulence parameters to be used in a Navier-Stokes solver.

The main research question that still holds is thus threefold. (i) Can we formulate efficient algorithms for self-consistent simulations of corona discharge in arbitrary configurations, eliminating the empirical assumptions and often severe limitations of simplified discharge models? (ii) How do such models perform when compared to

experimental measurements in terms of electrical characteristics and what is the influence of plasma-related tuning parameters, notably pre-ionization charge density levels? (iii) How do such models perform when compared to experimental measurements in terms of EAD flow characteristics and what is the influence of fluid-related tuning parameters, notably turbulence?

To this respect, this work presents two-dimensional axisymmetric (2D-axi), self-consistent plasma actuator simulations of a needle-to-ring corona discharge, under positive applied voltages and operating in relatively dry, atmospheric-pressure air. A complete plasma actuator simulation consists of two parts: a plasma discharge simulation performed with ONERA's in-house code COPAIER, and an ionic wind simulation performed with the open-source software OpenFOAM. The two (sub-)simulations are coupled in a one-way fashion in which the EAD force density, resulted from the plasma discharge simulation, is introduced as the source term into the momentum equation for the ionic wind simulation.

The structure of the article is as follows. First, we present the model methodology and essential modeling aspects (section 2) and the simulation case under study (section 3). Then numerical results of the steady-state discharge operation are presented, emphasizing on the resulting EAD spatial force density and voltage-current characteristics (section 4) as well as ionic wind profiles and voltage-velocity characteristics (section 5). The numerical results are compared with experiment data and various tuning parameters are analyzed in terms of their influence to the characteristics of the resulting ionic wind. Finally in section 6, we summarize our findings and provide future directions.

2. Methodology

2.1. Discharge model

For aeronautical applications, the drift-diffusion-Poisson equations are widely used to describe the discharge dynamics, in which participate numerous charged or neutral species.

Let $\mathfrak{S}$ be the set of species. For each specie $s \in \mathfrak{S}$, we denote as $n_s(t, \boldsymbol{x})$ the particle density at time t and position $\boldsymbol{x}$, $\boldsymbol{f}_s(t, \boldsymbol{x})$ the particle flux and $S_s(t, \boldsymbol{x})$ the production/decay source term of s. The electric potential and the electric field are resp. denoted as $\phi(t, \boldsymbol{x})$ and $\boldsymbol{E}(t, \boldsymbol{x})$ $(\equiv -\nabla\phi(t, \boldsymbol{x}))$.

In this study, we employ the kinetic scheme from [33] which consists of electrons (denoted as e), positive ions (p) and negative ions (n), i.e. $\mathfrak{S} = \{ e, p, n \}$. The source terms are given as follows [33],

$$\begin{cases} S_e = (\alpha - \eta) N n_e - k_{ep} n_e n_p, \\ S_p = \alpha N n_e - k_{ep} n_e n_p - k_{np} n_n n_p, \\ S_n = \eta N n_e - k_{np} n_n n_p, \end{cases} \tag{1}$$

where $\alpha(E/N)$, $\eta(E/N)$, $k_{ep}(E/N)$ and $k_{np}(E/N)$ are resp. the electron impact ionization, electron-neutral attachment, electron-ion recombination and ion-ion

recombination coefficients, while N and $E \equiv |\boldsymbol{E}|$ are resp. the air density‡ and electric field strength. The dependence of reaction coefficients (and drift-diffusion coefficients introduced later) on the reduced field strength E/N is derived from a local field approximation [39]. In this work, α and η are provided in look-up tables by the software BOLSIG+ [40], while k_{ep} and k_{np} are resp. set as 2×10^{-13} m^3 s^{-1} and 1.7×10^{-13} m^3 s^{-1}.

On another hand, a minimum constraint is imposed on the electron density - $n_e(t,\boldsymbol{x}) \geq \psi$ [41], where $\psi > 0$ is a user-defined parameter called floor density, simply taken as a constant (both in space and time) in this work. This constraint is introduced to fit numerical results to experimental measurements [27]; it can be viewed as an attempt to artificially include electron sources that are extremely diverse in reality, but numerically underrepresented in kinetic models such as (1), which are preferred to be as simple as possible for computational resource economy.

The discharge model writes in the following way,

$$\begin{cases} \partial_t \boldsymbol{U}(t,\cdot) + \nabla\cdot\boldsymbol{F}\left(\boldsymbol{E}(t,\cdot),\boldsymbol{U}(t,\cdot)\right) \in \boldsymbol{S}\left(E(t,\cdot),\boldsymbol{U}(t,\cdot)\right) + \boldsymbol{S}_\psi\left(\boldsymbol{U}(t,\cdot)\right), \\ \boldsymbol{U}(0,\boldsymbol{x}) = \boldsymbol{U}^0(\boldsymbol{x}), \\ -\nabla\cdot(\varepsilon_0\nabla\phi(t,\boldsymbol{x})) = \rho(t,\boldsymbol{x}), \end{cases} \tag{2}$$

where $\boldsymbol{U} \equiv (n_s)_{s\in\mathfrak{S}}$, $\boldsymbol{F} \equiv (\boldsymbol{f}_s)_{s\in\mathfrak{S}}$, $\boldsymbol{S} \equiv (S_s)_{s\in\mathfrak{S}}$, $\boldsymbol{S}_\psi \equiv (S_{\psi,s})_{s\in\mathfrak{S}}$, $\rho \equiv q\sum_{s\in\mathfrak{S}} z_s n_s$ is the net charge density, $\boldsymbol{U}^0(\boldsymbol{x}) \equiv (n_s^0(\boldsymbol{x}))_{s\in\mathfrak{S}}$ are initial data and ε_0 is the vacuum permittivity§, with $S_{\psi,e}(t,\cdot) \equiv -\partial I_{\mathcal{K}}(n_e(t,\cdot))$, $S_{\psi,s} = 0$ for $s \neq e$, q is the elementary charge‖ and z_s is the charge number of s¶. Boundary and initial conditions are omitted in this paper but can be found in [41].

Here, the set $\partial I_{\mathcal{K}}$ is the subdifferential [42] of the characteristic function $I_{\mathcal{K}}$,

$$I_{\mathcal{K}}(v) = \begin{cases} 0 & \text{if } v \in \mathcal{K}, \\ +\infty & \text{if } v \notin \mathcal{K}, \end{cases}$$

of the convex $\mathcal{K} = \{\, v \mid v(\boldsymbol{x}) \geq \psi \,\}$. The appearance of $\partial I_{\mathcal{K}}$ in the discharge model is to impose properly the aforementioned minimum constraint $n_e \geq \psi$ [41]; consequently, the conservation laws are in the form of differential inclusions.

Finally, the particle fluxes $\boldsymbol{f}_s$ satisfy a mobility law as follows,

$$\begin{cases} \boldsymbol{f}_s = \boldsymbol{u}_s n_s - D_s\nabla n_s, \\ \boldsymbol{u}_s = \mathrm{sign}(z_s)\mu_s\boldsymbol{E}, \end{cases}$$

where $\mu_s(E/N)$ and $D_s(E/N)$ are resp. the mobility and diffusion coefficients, which are also precomputed by the software BOLSIG+ [40].

‡ $N = 2.5\times10^{25}$ m^{-3} in this study
§ $\varepsilon_0 = 8.854\times10^{-12}$ C V^{-1} m^{-1} in this study
‖ $q = 1.602\times10^{-19}$ C in this study
¶ $z_e = -1$, $z_p = +1$, $z_n = -1$

2.2. Numerical modeling of positive corona discharges

The numerical simulations are conducted with ONERA's multi-reactions, multi-species parallelized plasma solver COPAIER [38] on two-dimensional triangular grids $\mathcal{T}_h \equiv (\Omega_K)_{K=1,\dots,\mathcal{L}}$, generated by the software Gmsh [43]. Some features of the numerical schemes, on the discretization of the discharge model (2), are presented in this section. For further details, we refer to [38, 41].

Let $0 = t^0 < t^1 < \ldots < t^{\mathcal{N}} = T$ be a partition of the time interval $[0, T]$. For $0 \leq l \leq \mathcal{N}$, let $f^l(\boldsymbol{x})$ be an approximation of $f(t^l, \boldsymbol{x})$ at t^l for any scalar or vector-valued variable f. We consider the following implicit time discretization of (2),

$$\left\{ \begin{array}{l} \dfrac{\boldsymbol{U}^{l+1} - \boldsymbol{U}^l}{\Delta t^l} + \nabla \cdot \boldsymbol{F}(\boldsymbol{E}^l, \boldsymbol{U}^{l+1}) \in \boldsymbol{S}(E^l, \boldsymbol{U}^l, \boldsymbol{U}^{l+1}) + \boldsymbol{S}_\psi(\boldsymbol{U}^{l+1}), \\ \nabla \cdot (\varepsilon_0 \nabla \boldsymbol{E}^{l+1}) = \rho^{l+1}, \end{array} \right. \tag{3}$$

with $\Delta t^l \equiv t^{l+1} - t^l$ for $0 \leq l < \mathcal{N}$, and

$$\boldsymbol{S}(E^l, \boldsymbol{U}^l, \boldsymbol{U}^{l+1}) \equiv \begin{pmatrix} (\alpha^l - \eta^l) N n_e^{l+1} - k_{ep}^l n_e^{l+1} n_p^l \\ \alpha^l N n_e^{l+1} - k_{ep}^l n_e^{l+1} n_p^l - k_{np}^l n_n^l n_p^l \\ \eta^l N n_e^{l+1} - k_{np}^l n_n^l n_p^l \end{pmatrix}. \tag{4}$$

The discretization (3) allows to update separately the particle densities $\boldsymbol{U}^{l+1}$ and the electric field $\boldsymbol{E}^{l+1}$. Taking advantage of the slow-varying electric field in positive corona discharges, the numerical timesteps are defined as

$$\Delta t^l = \min(\mathfrak{C} \Delta t_i^l, \Delta t_\phi^l), \tag{5}$$

where $\mathfrak{C} > 0$ is a user-defined parameter, Δt_i^l and Δt_ϕ^l are resp. the CFL timestep of ions and the dielectric relaxation timestep, given as

$$\Delta t_i^l = \min_{K, s \in \mathfrak{S} \setminus \{e\}} \left(\frac{h_K}{|\boldsymbol{u}_{s,K}^l|} \tanh\left(\frac{|\boldsymbol{u}_{s,K}^l| h_K}{2 D_{s,K}^l} \right) \right),$$

$$\Delta t_\phi^l = \min_K \left(\frac{\varepsilon_0}{q \sum_{s \in \mathfrak{S}} |z_s| \mu_{s,K}^l n_{s,K}^l} \right),$$

where h_K is the size of the triangle Ω_K while f_K^l is an approximation of any variable f at t^l and the center of Ω_K.

In our simulations, $\mathfrak{C}$ is set at 10^3, knowing that $\Delta t_i^l \ll \Delta t_\phi^l$ more than often in positive corona discharges. Moreover, structure of (4) facilitates the resolution of (3), the nonlinearity of the system being only brought into the first line of (3) by the term $\boldsymbol{S}_\psi(\boldsymbol{U}^{l+1})$. In order to deal with this nonlinearity, we have developed a Gauss-Seidel-inspired algorithm in [41].

In the previous study [41], the implicit discretization (3)-(4) allowed us to compute a positive wire-to-wire corona discharge in about five hours on 4 processors, instead of a week if using an explicit time scheme[+]. In this paper, each simulation of the positive needle-to-ring discharge, described in section 3, takes about three to five hours to

[+] RK2-Heun scheme [38]

complete on a mesh with 178000 to 187000 elements, partitioned between 32 processors (MPI parallelization).

2.3. Computation of EAD jets

After simulating the discharge, we inject the steady-state EAD force density, $\boldsymbol{F}_{\text{EAD}} \equiv \rho_0 \boldsymbol{E}$, into the homogeneous, incompressible Navier-Stokes equations to compute the induced EAD jet. More precisely, we solve for the steady-state CFD solutions (velocity $\boldsymbol{u}$ and kinematic pressure p) of the following system [44, Chapter 2],

$$\begin{cases} \nabla \cdot \boldsymbol{u} = 0, \\ \nabla \cdot (\boldsymbol{u} \otimes \boldsymbol{u}) - \nabla \cdot (\overline{\nu} \nabla \boldsymbol{u}) - \nabla \overline{\nu} \cdot \nabla \boldsymbol{u} = -\nabla p + \dfrac{\boldsymbol{F}_{\text{EAD}}}{\rho_0}, \end{cases} \tag{6}$$

where $\otimes$ is the Kronecker tensor product, $\overline{\nu}(\boldsymbol{x})$ is the effective kinematic viscosity, p is the kinematic pressure and ρ_0 is the volumetric mass of air*.

The coupling between the discharge and the ionic wind is, thus, assumed to be one-way, which means that the discharge affects the jet but not the other way around since the jet velocity is low and the discharge timescale is much smaller than the flow timescale.

The form of $\overline{\nu}$ depends on the CFD models. In this paper we consider two of them.

(i) *Laminar model.* Here, the effective kinematic viscosity is simply the kinematic viscosity of air ν_0, which is assumed to be constant and set to 1.48×10^{-5} m^2 s^{-1} in this study,

$$\overline{\nu} = \nu_0. \tag{7}$$

(ii) *Realizable k-ε turbulence model.* $\overline{\nu}$ is defined as, with $\nu_t(\boldsymbol{x})$ being the kinematic turbulence eddy viscosity,

$$\overline{\nu} = \nu_0 + \nu_t, \quad \nu_t = C_\nu \frac{k^2}{\varepsilon}. \tag{8}$$

Here, $k(\boldsymbol{x})$ and $\varepsilon(\boldsymbol{x})$ are resp. the turbulence kinetic energy per unit mass and the turbulence kinetic energy dissipation rate. Their equations, as well as the definition of the coefficient $C_\nu(\boldsymbol{x})$ in (8), can be found in Appendix A.

The system (6)-(7) or (6)-(8) are solved by the CFD software OpenFOAM [46], with proper boundary conditions which are precised in Appendix A. Among those, we are most interested in the inlet boundary conditions of k and ε, which are given by [44, Chapter 7]

$$k_{\text{in}} = \frac{3}{2}(I_{t,\text{in}} u_0)^2, \quad \varepsilon_{\text{in}} = \frac{C_\mu^{\frac{3}{4}} k_{\text{in}}^{\frac{3}{2}}}{l_m}, \tag{9}$$

where k_{in} and ε_{in} are resp. the values of k and ε on inlet boundaries, $I_{t,\text{in}}$ is the inlet turbulence intensity, u_0 is the inlet flow velocity, $C_\mu = 0.09$ and l_m is the Prandtl mixing length.

* $\rho_0 = 1.17972$ kg m^{-3} in this study (at 1 atm, 25°C and 30% relative humidity as in [45])

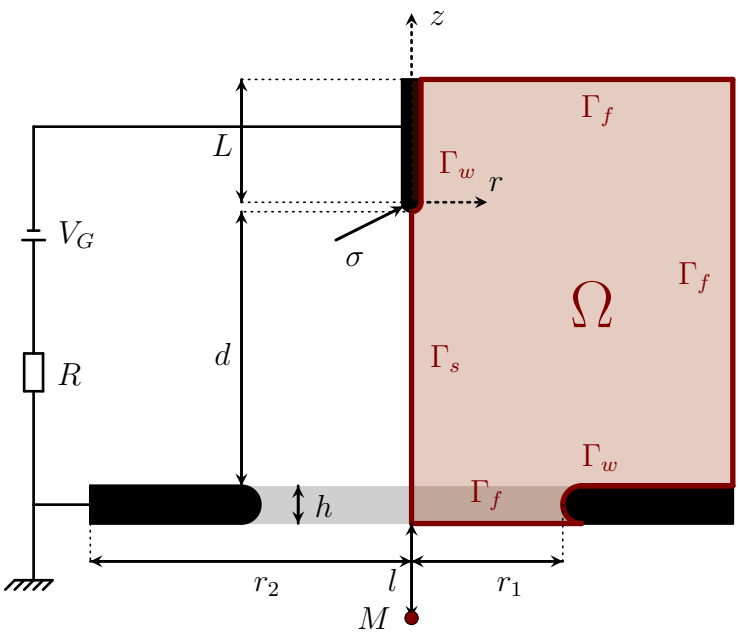

Figure 1: Sketch of the needle-to-ring actuator (not scaled to size), where the computation domain Ω, for plasma discharge simulations, is colored in maroon (details on the boundaries Γ_f, Γ_s, Γ_w can be found in [41])

The inlet conditions k_{in} and ε_{in} have a huge impact on the numerical results, namely the EAD jet velocity $\boldsymbol{u}$, as we will show in section 5.4. The values of the parameters in (9) will be stated in section 3. Note that the values of $I_{t,\text{in}}$ and l_m will be fixed, so that only the value of u_0 will be adjusted.

3. Description of the studied needle-to-ring actuator

A sketch of the device, which was studied in [45], is shown in fig. 1. The actuator is composed of a small metal needle and a metal ring. Here, σ, r_1, r_2 and d are resp. the curvature of the needle tip, the inner and outer radii of the ring, and the electrode gap. The simulations are conducted in cylindrical coordinates $\boldsymbol{x} = (r, z)$.

A high potential $V_G > 0$ is applied to the needle while the ring is grounded. The ignition voltage V_c for different electrode gaps d were measured experimentally in [45] and are relisted in table 1 for $V_G > 0$. The overvoltage is defined as $\Delta V_G = V_G - V_c$. To avoid the formation of positive streamers during the discharge ignition, we increase gradually the voltage on 10 μs until it reaches the maximal value V_G, then keep this value until the simulation time $T = 4$ ms.

The grid is particularly refined near the needle tip to capture correctly the discharge dynamics, as shown in fig. 2. The minimal grid size for all simulations is $\Delta x_{\min} = 4.5$ μm.

For the CFD simulations, we evaluate the EAD jet velocity at a point M on the

d (mm)	20	25	30
V_c (kV)	7.1	7.4	8.0

Table 1: Experimentally measured ignition voltage V_c for positive polarity for different electrode gaps d [45]

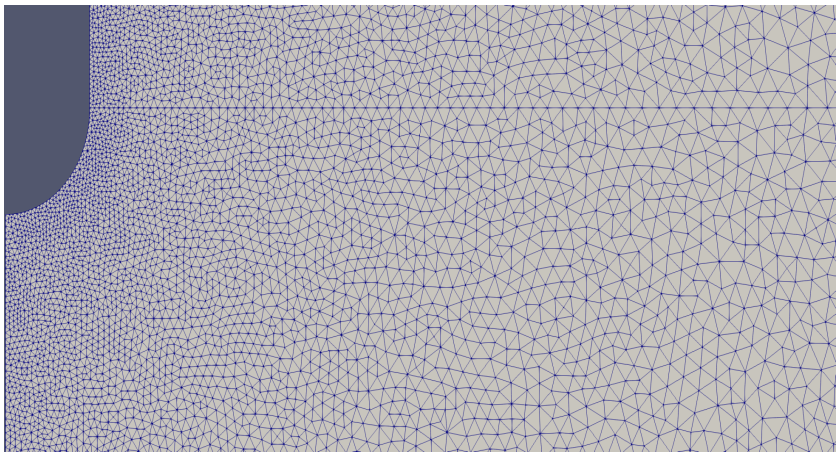

Figure 2: Grid refinement near the needle tip, generated by Gmsh [43]

σ	0.1 mm	L	5 mm	ΔV_G	2-14 kV	$I_{t,\text{in}}$	1%
r_1	10 mm	l	5 mm	R	20 kΩ	l_m	1 mm
r_2	20 mm	h	2 mm	T	4 ms	u_0	3-60 m s^{-1}
d	20-30 mm	$\Delta x_{\min}$	4.5 μm	ψ	10^9-10^{12} m^{-3}		

Table 2: Actuator characteristics and numerical parameters

symmetry axis, at a distance l downstream from the ring (see fig. 1). The parameters in (9) for the turbulence inflow boundary conditions are chosen as $I_{t,\text{in}} = 1\%$, $l_m = 5\% \times 2r_1$ and u_0 ranging from 3 to 60 m s^{-1}.

Actuator characteristics as well as numerical parameters, for the simulations in section 4, are listed in table 2. By default, we choose $d = 20$ mm, $\psi = 10^{11}$ m^{-3} (the floor density) and $u_0 = 50$ m s^{-1}, unless stated otherwise.

4. Numerical results and discussion on plasma discharge

4.1. Characteristics of steady-state positive needle-to-ring discharge

Figure 3 shows the positive ion density n_p as well as the electron density n_e in log scale, for $\Delta V_G = 12$ kV, at steady state ($T = 4$ ms). The typical particle distribution in a corona discharge can be observed, as the charges are heavily concentrated in the anode region around the needle tip, and expand gradually towards other directions. Effects

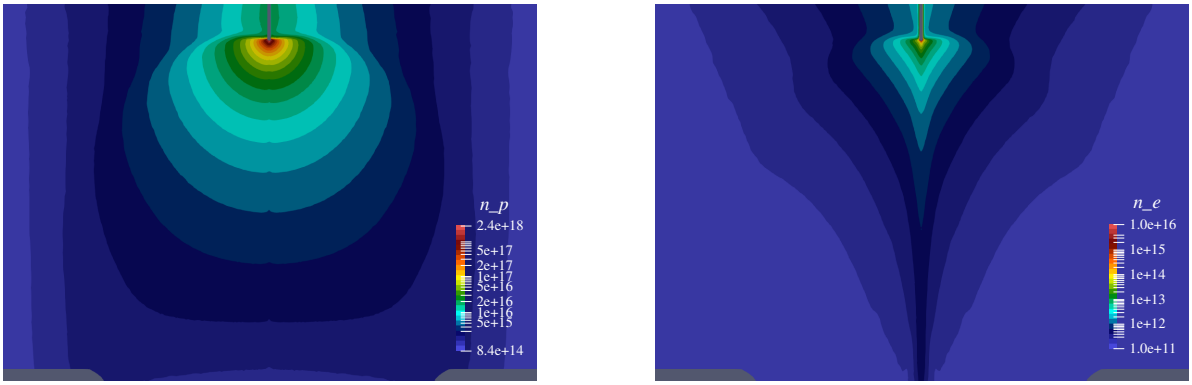

(a) n_p (m^{-3}) (b) n_e (m^{-3})

Figure 3: Positive ion and electron densities for $d = 20$ mm, $\psi = 10^{11}$ m^{-3} and $\Delta V_G = 12$kV in log scale (the computation domain was reflected with respect to the symmetry axis $r = 0$)

of the actuator geometry can also be seen on the electrons as the contour lines of n_e are "squeezed" by the ring since they bear the same charge sign, and less visibly, on the positive ions as the cathode creates small splits near the symmetry axis $r = 0$ on the contour lines of n_p.

Figure 4 provides more enhanced views of the anode region for $\Delta V_G = 12$ kV in normal scale. The positive ions at the steady state accumulate in front of the needle tip with a density up to 2.5×10^{18} m^{-3}. The density of other species are negligible comparing to n_p as n_e and n_n are on the order of 10^{16} m^{-3}. Therefore, positive ions account for most of the EAD force.

It is shown more clearly that the contour lines of n_p form a bell-pepper-like structure instead of a horseshoe such as in a needle-to-plane discharge. The radial position of the maximum of n_p in this needle-to-ring discharge is located around $r = 0.01$ mm rather than on the symmetry axis. Furthermore, we can also notice an annular structure (in 3D) around the tip around $r = 0.125$ mm with n_p about 1.5×10^{18} m^{-3}. On another hand, the electric field lines E are quite smooth as in a typical positive corona discharge.

For different voltages ΔV_G in the case $d = 20$ mm and $\psi = 10^{11}$ m^{-3}, the positive ion and electron densities are displayed in fig. 5 and the r- and z-components F_r, F_z of the EAD force density $\boldsymbol{F}_{\mathrm{EAD}} \equiv \rho \boldsymbol{E}$ are displayed on fig. 6. The morphology of particle distributions is quite the same for all values of ΔV_G - a low voltage 4 kV, a moderate voltage 8 kV and a high voltage 12 kV. A notable difference is that the particle densities increase significantly with the voltage as expected. The same remarks are also relevant for the morphology and intensity of $\boldsymbol{F}_{\mathrm{EAD}}$.

On the other hand, the morphology of particle distributions and EAD force density is strongly affected by the electron floor density ψ. Figures 7 and 8 displays this effect on n_p, n_e, F_r and F_z for $\psi = 10^9$, 10^{11} and 10^{12} m^{-3}, in the case $d = 20$ mm and $\Delta V_G = 12$ kV. We can observe that the charge distributions, especially that of positive ions, is

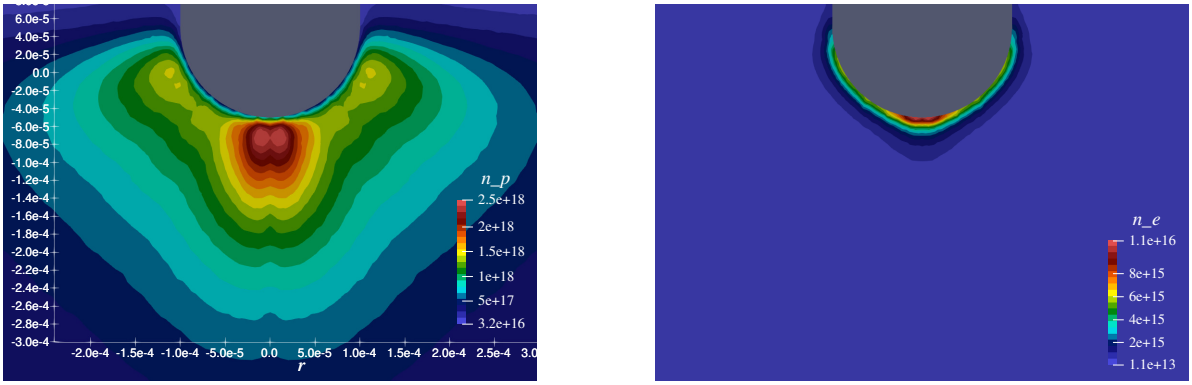

(a) n_p (m^{-3}) (b) n_e (m^{-3})

(c) n_n (m^{-3}) (d) E (V m^{-1})

Figure 4: Particle densities and electric field strength for $d = 20$ mm, $\psi = 10^{11}$ m^{-3} and $\Delta V_G = 12$ kV

more irregular the lower the floor density is. This phenomenon is perhaps due to the large gradient of n_e when ψ is small.

Since positive ions are responsible for most of the EAD force, the morphology of $\boldsymbol{F}_{\mathrm{EAD}}$ is also more rugged as ψ decreases. Because of the annular structure of n_p around $r = 0.125$ mm, the EAD force density has a significant r-component that acts on the outward direction from the needle. The maximum strength of this radial force is from two-fifth to three-fifth of that of the axial force.

The levels of n_p, is roughly on the same order for all values of ψ. However, the axial position of the maximum of n_p is closer to the needle as the floor density is smaller, as shown in fig. 9. This enhances the electric field in the anode region, so as a consequence, the EAD force density. We can note from fig. 7 that $\boldsymbol{F}_{\mathrm{EAD}}$ is the strongest for $\psi = 10^9$ m^{-3}.

4.2. Electric current and comparison with experiment data - the V-I curves

The potential-current characteristics (V-I curves) of the discharge are shown on fig. 10 for different values of ψ. The analytic expression of the discharge current I in the

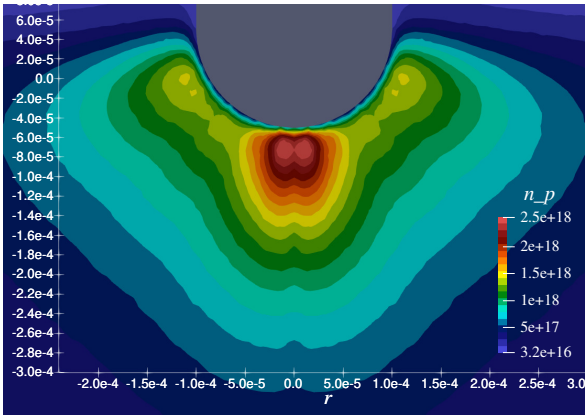

(a) n_p (m^{-3}), $\Delta V_G = 12$ kV

(b) n_e (m^{-3}), $\Delta V_G = 12$ kV

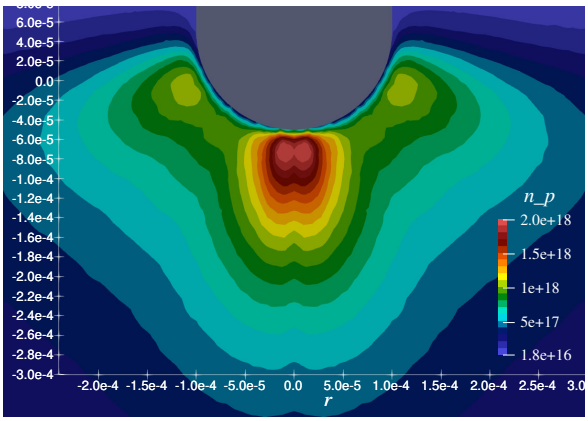

(c) n_p (m^{-3}), $\Delta V_G = 8$ kV

(d) n_e (m^{-3}), $\Delta V_G = 8$ kV

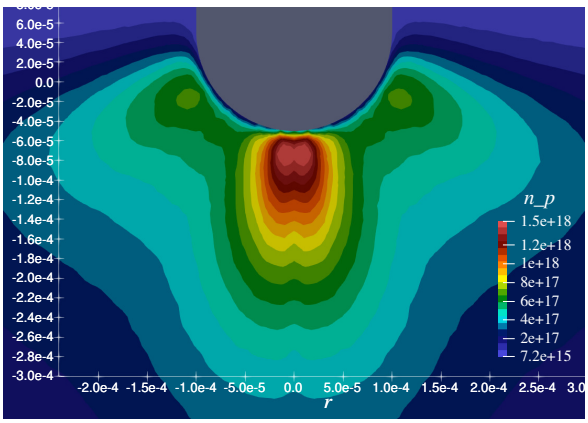

(e) n_p (m^{-3}), $\Delta V_G = 4$ kV

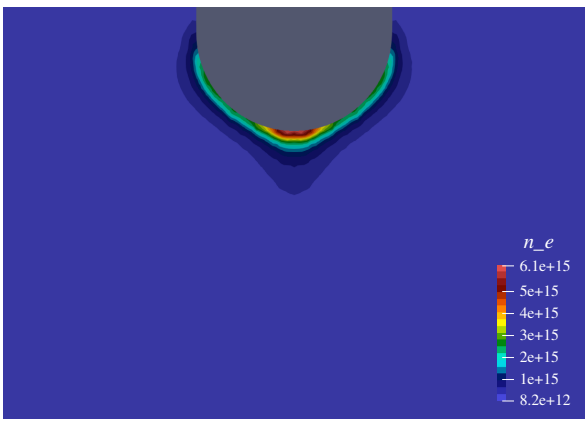

(f) n_e (m^{-3}), $\Delta V_G = 4$ kV

Figure 5: Positive ion and electron densities for $d = 20$ mm, $\psi = 10^{11}$ m^{-3} and different values of ΔV_G

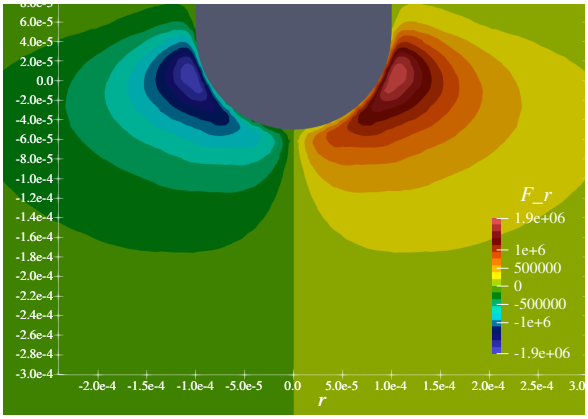

(a) F_r (N m^{-3}), $\Delta V_G = 12$ kV

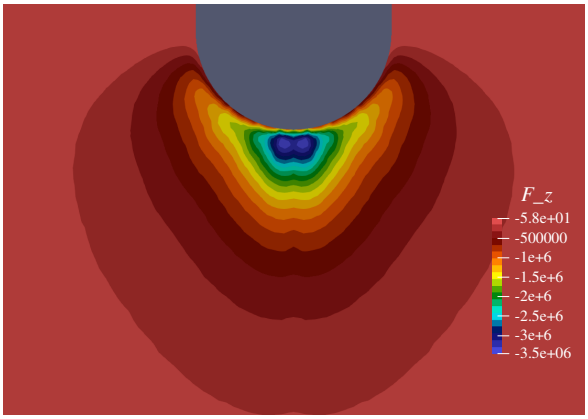

(b) F_z (N m^{-3}), $\Delta V_G = 12$ kV

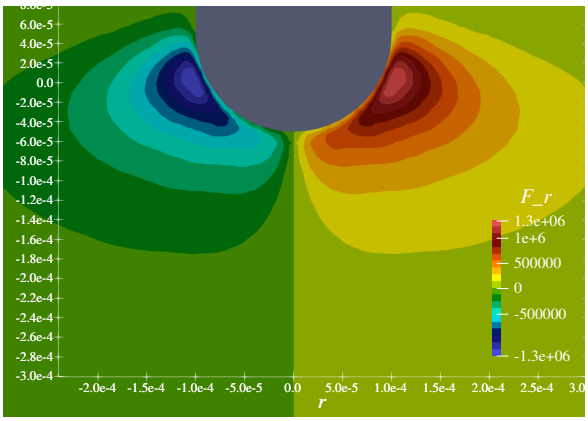

(c) F_r (N m^{-3}), $\Delta V_G = 8$ kV

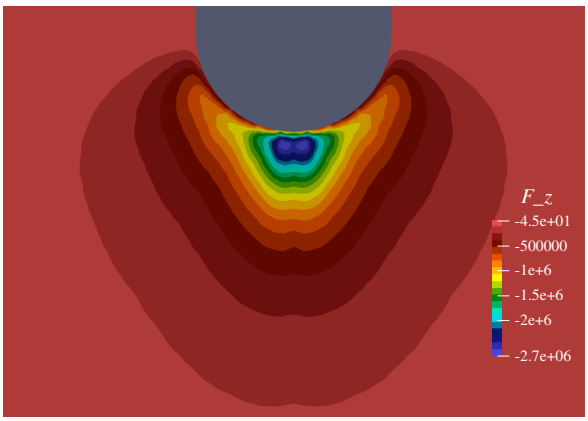

(d) F_z (N m^{-3}), $\Delta V_G = 8$ kV

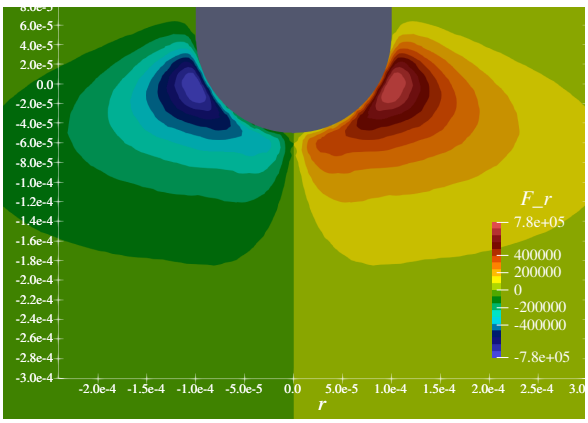

(e) F_r (N m^{-3}), $\Delta V_G = 4$ kV

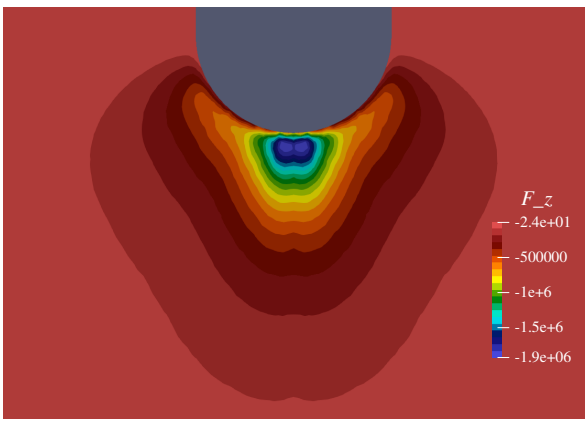

(f) F_z (N m^{-3}), $\Delta V_G = 4$ kV

Figure 6: Components of the EAD force density for $d = 20$ mm, $\psi = 10^{11}$ m^{-3} and different values of ΔV_G

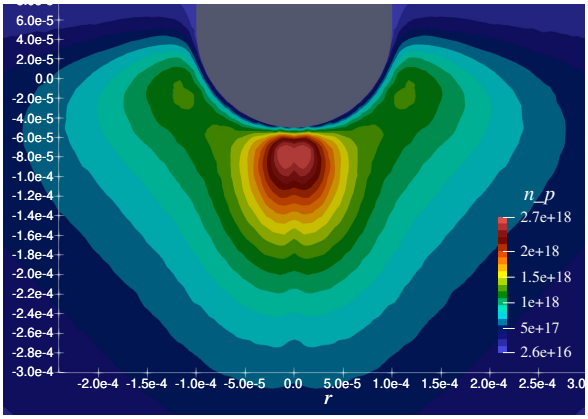

(a) n_p (m^{-3}), $\psi = 10^{12}$ m^{-3}

(b) n_e (m^{-3}), $\psi = 10^{12}$ m^{-3}

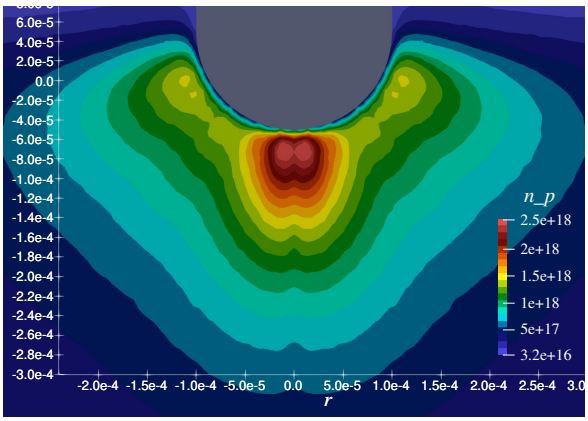

(c) n_p (m^{-3}), $\psi = 10^{11}$ m^{-3}

(d) n_e (m^{-3}), $\psi = 10^{11}$ m^{-3}

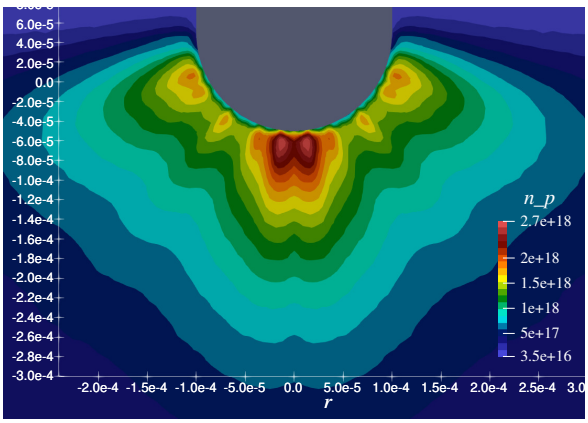

(e) n_p (m^{-3}), $\psi = 10^{9}$ m^{-3}

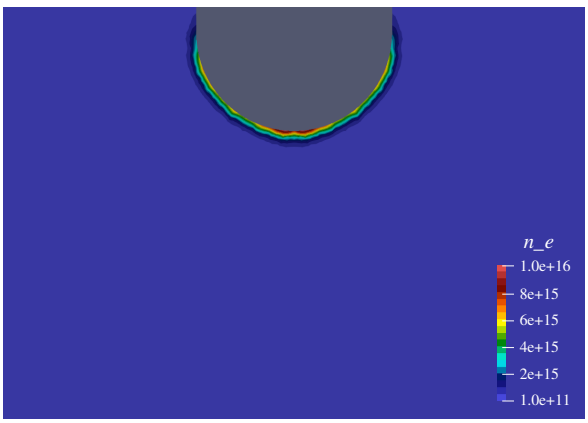

(f) n_e (m^{-3}), $\psi = 10^{9}$ m^{-3}

Figure 7: Positive ion and electron densities for $d = 20$ mm, $\Delta V_G = 12$ kV and different values of ψ

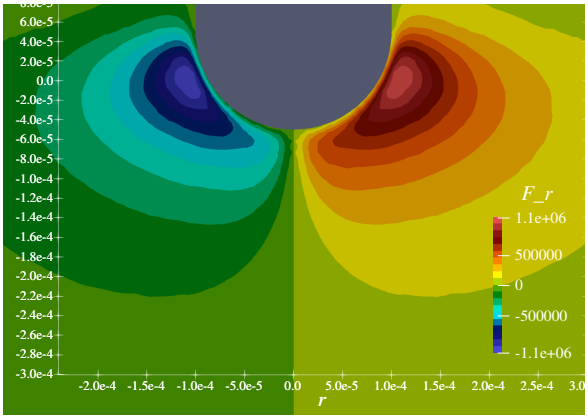

(a) F_r (N m^{-3}), $\psi = 10^{12}$ m^{-3}

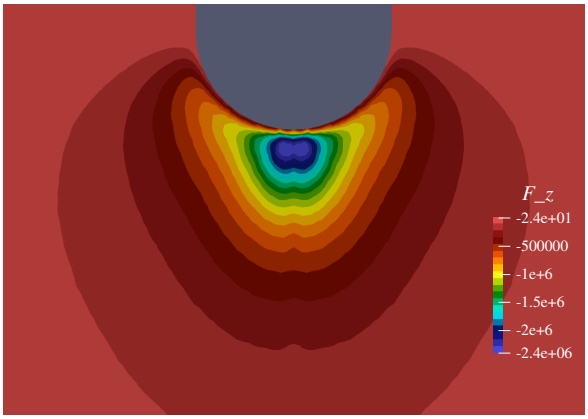

(b) F_z (N m^{-3}), $\psi = 10^{12}$ m^{-3}

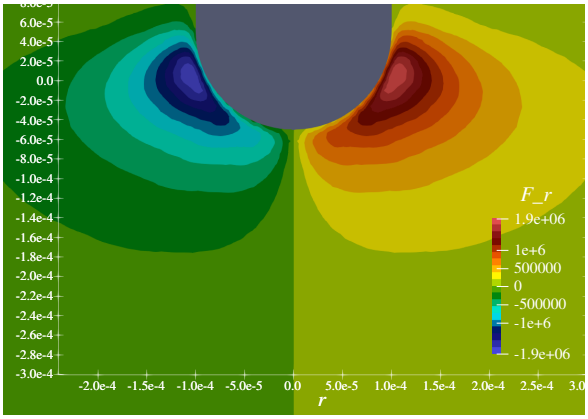

(c) F_r (N m^{-3}), $\psi = 10^{11}$ m^{-3}

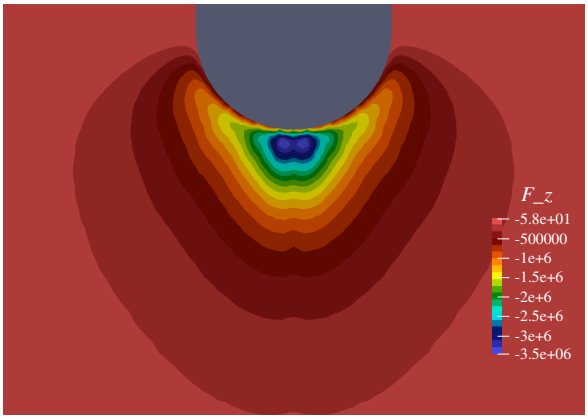

(d) F_z (N m^{-3}), $\psi = 10^{11}$ m^{-3}

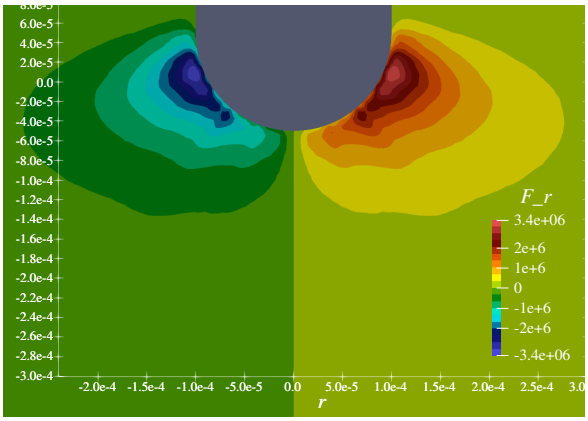

(e) F_r (N m^{-3}), $\psi = 10^{9}$ m^{-3}

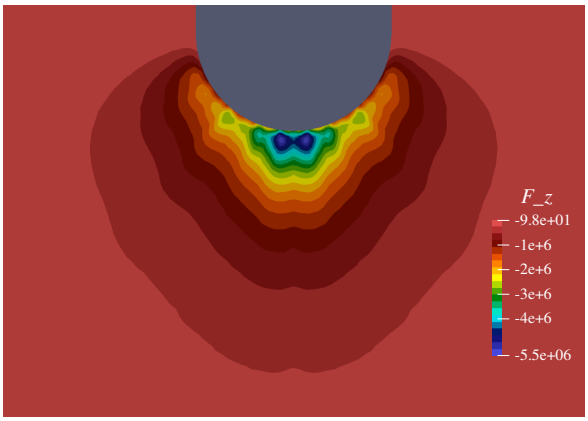

(f) F_z (N m^{-3}), $\psi = 10^{9}$ m^{-3}

Figure 8: Components of the EAD force density for $d = 20$ mm, $\Delta V_G = 12$ kV and different values of ψ

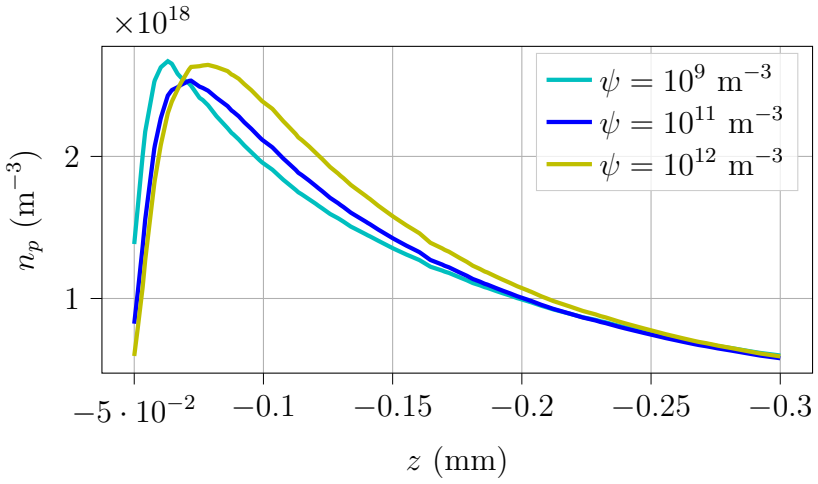

Figure 9: Positive ion density at $r = 0.01$ mm for $d = 20$ mm, $\Delta V_G = 12$ kV and different values of ψ. The needle tip is located at $z = -0.05$ mm.

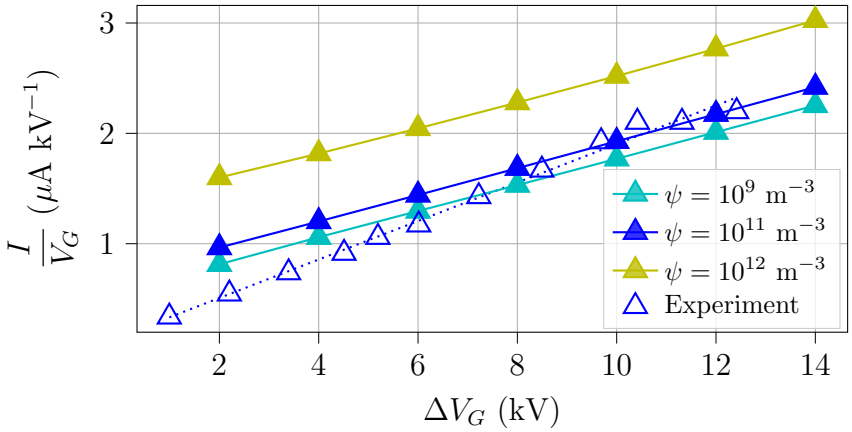

Figure 10: Comparison of V-I curves for $d = 20$ mm between numerical solutions (with different values of ψ) and experiment data available in [45]. The dotted blue line is the fitting of experiment data following the law (10).

	Experiment	$\psi = 10^9$ m^{-3}	$\psi = 10^{11}$ m^{-3}	$\psi = 10^{12}$ m^{-3}
k_{VI} (μA kV^{-2})	0.174	0.12	0.121	0.119

Table 3: V-I characteristics of experimental data [45] and numerical solutions (with different values of ψ) for $d = 20$ mm

electric circuit can be found in [26]. Using a quadratic fitting for the curves, we found that the V-I characteristics satisfy the empirical law

$$\frac{I}{V_G} = k_{VI}\Delta V_G, \tag{10}$$

where the proportionality coefficients $k_{VI} > 0$ are listed in table 3.

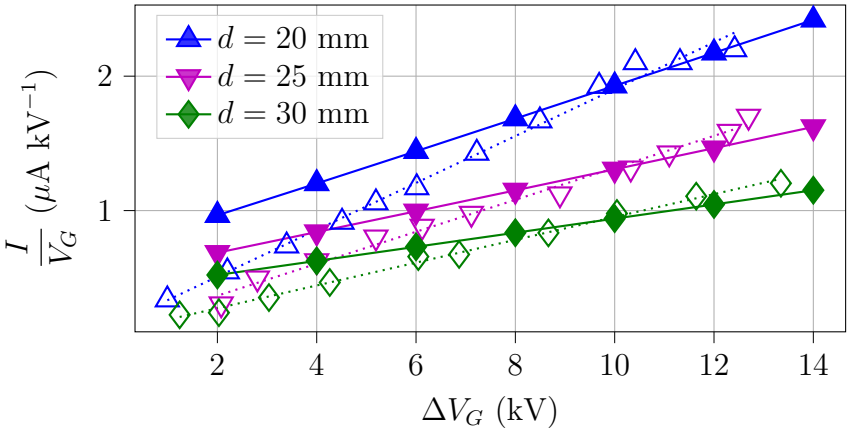

Figure 11: V-I curves of numerical solutions (filled markers) and experiment data [45] (hollow markers) for different values of d. The dotted lines are the fittings of experiment data following the law (10).

	$d = 20$ mm		$d = 25$ mm		$d = 30$ mm	
	Experiment	$\psi = 10^{11}$ m^{-3}	Experiment	$\psi = 10^{11}$ m^{-3}	Experiment	$\psi = 10^{11}$ m^{-3}
k_{VI} (μA kV^{-2})	0.17	0.12	0.12	0.08	0.08	0.05

Table 4: V-I characteristics of experiment data [45] and numerical solutions for different values of d

Overall, the coefficients k_{VI} computed from the numerical solutions are practically the same for all considered values of ψ but differ slightly from the experiment data [45]. Since the curve of $\psi = 10^{11}$ m^{-3} seems to fit the experiment data better than $\psi = 10^{9}$ m^{-3} for high values of ΔV_G (in the range of 10-12 kV), we choose $\psi = 10^{11}$ m^{-3} for the following simulations.

Figure 11 presents the V-I characteristics for different values of d. As for $d = 20$ mm, the coefficients k_{VI} computed for $d = 25$ and 30 mm also differ slightly from experiment data available in [45] - see table 4. This discrepancy was also observed in our previous study on a positive wire-to-wire discharge [41], especially when the radius of the stressed electrode is large, indicating that the discharge current is sensitive to many factors, such as chemical composition of the gas, impurities on the electrode surface, experimental configuration linked to the high voltage generator and ground elements around the device, etc.

Therefore, we propose to study the EAD effects of the discharge, since the ionic wind should be less affected by small disturbances of discharge conditions, owing to its considerably larger physical timescale (on the order of 1 ms) comparing to that of the discharge itself (0.1 ms).

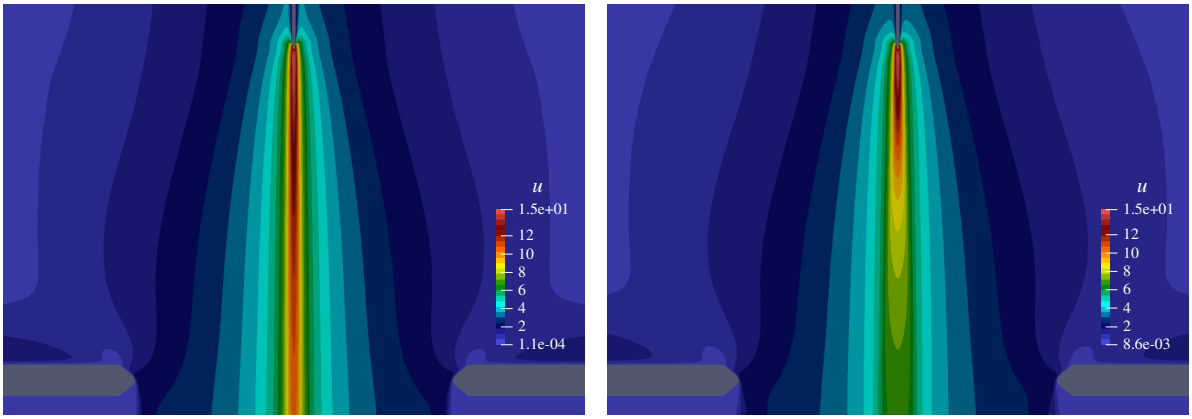

(a) Laminar jet (b) Turbulent jet with $u_0 = 50$ m s^{-1}

Figure 12: EAD jet velocity u (m s^{-1}) computed with different CFD models for $d = 20$ mm and $\Delta V_G = 12$ kV

5. Numerical results and discussion on ionic wind

5.1. Are EAD jets laminar or turbulent flows?

In this section, we discuss the difference on the computed flow velocity $u \equiv |\boldsymbol{u}|$ obtained with the laminar NS equations - eqs. (6) and (7) - and the turbulence model - eqs. (6) and (8). For the latter, different values of the inlet flow velocity u_0, which appears in inlet boundary conditions (9) of k and ε, are prescribed for the simulations with the intention of matching the experiment measurements available in [45].

The difference in morphology between a laminar and a turbulent jet is noticeable. On fig. 12, it is shown that while the maximum of the jet velocity magnitude $u \equiv |\boldsymbol{u}|$ is the same, the turbulent flow is much more diffusive (for $u_0 = 50$ m s^{-1}), due to the eddy viscosity injected on the inlet boundary. Indeed, the downstream jet velocity of the turbulent flow, at the center of the ring, is only roughly half of that of the laminar flow.

For a more quantitative comparison, we plot on fig. 13 the profiles of u at $z = -(\sigma + d + h + l)$ - or at the distance l downstream of the cathode‡ - for $d = 20$ mm, $\Delta V_G = 12$ kV and $\psi = 10^{11}$ m^{-3}. The data from simulations with the turbulence model are marked by their respective inlet velocity u_0.

The first observation is that the laminar model overestimates significantly the jet velocity comparing to the experiment data in the "jet core" - that is the zone within $r < 2$ mm - with a factor of about 5/3 between the maximum values of the jet velocity. Using the turbulence model with a small inlet velocity, for example $u_0 = 3$ m s^{-1}, does not "correct" the overestimation. By only increasing u_0, and therefore the inlet turbulence viscosity, the numerical result begins to match the experiment measurements in the jet core. This observation shows that positive-corona-induced EAD jets are likely of

‡ in [45], the distance l is said to be "between the discharge part and the Anemometer"; we assume it to be between the cathode bottom surface and the measure line in this study

turbulent nature, which is in accordance with previous studies' conclusion [47, 48, 49] for other geometries. This conclusion is also supported by looking at the turbulence intensity which will be addressed later in section 5.2.

The best matching results that we obtain in this case, in terms of the maximum value of u, are for $u_0 = 50$ m s^{-1} (see again fig. 13) - with $\max u_0 = 6.46$ m s^{-1} - and for $u_0 = 60$ m s^{-1} - with $\max u_0 = 5.79$ m s^{-1} - knowing the experimental value of 6.19 m s^{-1}. Therefore, we will set $u_0 = 50$ m s^{-1} in subsequent simulations.

The second observation is that the simulations always overestimate the flow velocity outside the jet core (i.e. $r > 2$ mm), no matter what CFD models used in this study. There exist many factors that could affect the exactitude of the results: measurement operating conditions, actuator geometry§, impurities on electrode surfaces, charge collection from other surfaces around the device, etc. The numerical results presented in Appendix B eliminate some geometry-related factors, but fail to reduce the simulation-experiment discrepancy.

The final observation that we can make is that the value of u_0 that gives the best result - $u_0 = 50$ m s^{-1} - is unusually high. Indeed, u_0 can be understood as the reference flow velocity of the air sucked into the domain by the actuator, which cannot be that high since the maximal jet velocity on the whole domain is only about 15 m s^{-1} (see fig. 12). As a matter of fact, the jet velocity near the inlet boundary that is obtained with any simulations in this case is less than 4 m s^{-1}. This observation, combining with the fact that the realizable k-ε model or any RANS models are primarily suited to describe fully turbulent flows, is a sign implicating that corona-induced EAD jets are of laminar-turbulent transitional nature - a conclusion also made in [48].

Therefore, the use of any RANS model seems to be not well adapted for such flows - more complicated analysis (e.g with LES, DNS or even transitional turbulent models) requires a dedicated study and largely increases the computational cost. In the application of the turbulence model (6)-(8) in the simulations of this work, the inlet velocity u_0 as well as the induced turbulence viscosity are tuning parameters with no real physical sense. They are modulated to artificially "inject" information of the development of eddies into the simulations, which was lost through the averaging process in the turbulence model, in order to recover the experiment data.

5.2. Turbulence indicators

Two parameters are used in this study to determine, in a more quantitative way, the turbulent nature of a flow. The first one is the ratio $r_\nu(\boldsymbol{x})$ between the eddy viscosity and the viscosity of air, i.e.

$$r_\nu = \frac{\nu_t}{\nu_0}.$$

§ in [45], the details of the geometry which are not known (despite having contacted and inquired the authors of the experimental work), for example the needle length, the needle skew angle, the ring thickness, the ring curvature; all of these could influence the numerical results

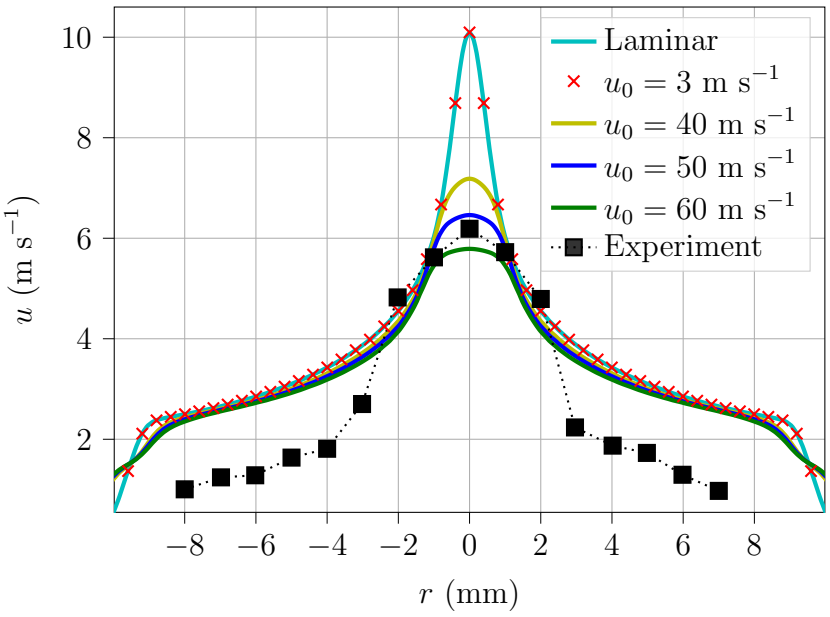

Figure 13: EAD jet velocity at $z = -27.1$ mm - or 5 mm downstream of the cathode - for $d = 20$ mm and $\Delta V_G = 12$ kV. Comparison between the laminar model, the turbulence model (with different values of u_0) and experiment data [45].

On figs. 14 and 15, we plot r_ν on the symmetry axis $r = 0$ with $-(\sigma + d + h + l) \leq z \leq -0.11$ mm, resp. for different values of ΔV_G and different values of d. The ratio reaches 10-200 at the end of the computation domain, depending on the case, but is near zero near the needle tip‖. Hence, it confirms, in addition to the observations made in section 5.1, the laminar-turbulent transitional nature of corona-induced EAD jets. Overall, r_ν is higher for smaller ΔV_G or larger d.

The second turbulence indicator is the turbulence intensity, $I_t(\boldsymbol{x})$, which has no unit and is defined as follows,

$$I_t = \left(\frac{2}{3}\frac{k}{u^2}\right)^{\frac{1}{2}},$$

where k is the turbulence kinetic energy per unit mass and u is the local flow velocity magnitude.

On figs. 16 and 17, we plot I_t on the symmetry axis $r = 0$ with $-(\sigma+d+h+l) \leq z \leq -0.11$ mm, resp. for different values of ΔV_G and different values of d. The turbulence intensity reaches 50-60% near the needle tip then drops to about 5% around $z = -1$ mm and gradually increases further downstream. The downstream intensity level depends on the case, which can be as low as 10% and as high as 40% but also indicates that EAD jets are turbulent flows¶. Overall, I_t is higher for smaller ΔV_G or larger d.

‖ located at $r = 0$, $z = -\sigma = -0.1$ mm

¶ however, I_t is not necessary a reliable turbulence indicator, since one can have high k level with high ε values leading to weak values of ν_t

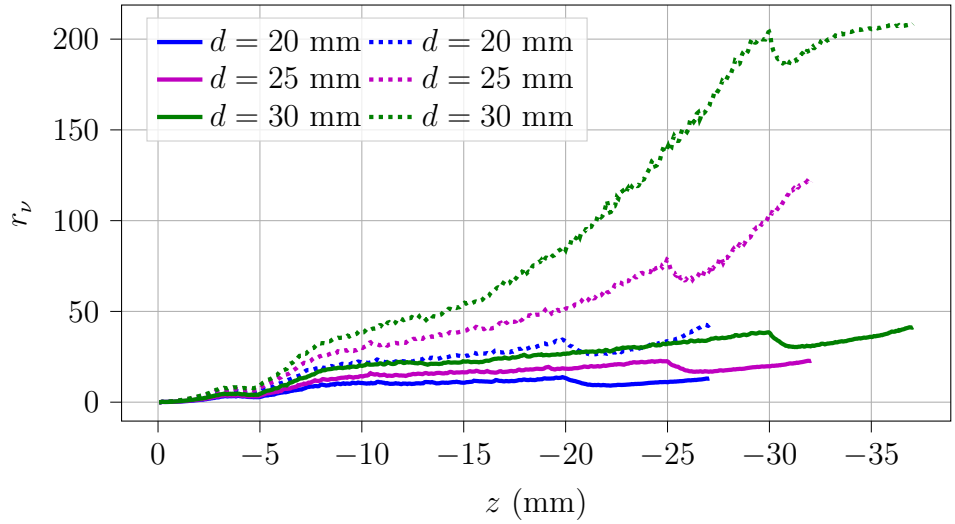

Figure 14: Turbulence intensity on symmetry axis for $d = 20$ mm and different values of ΔV_G

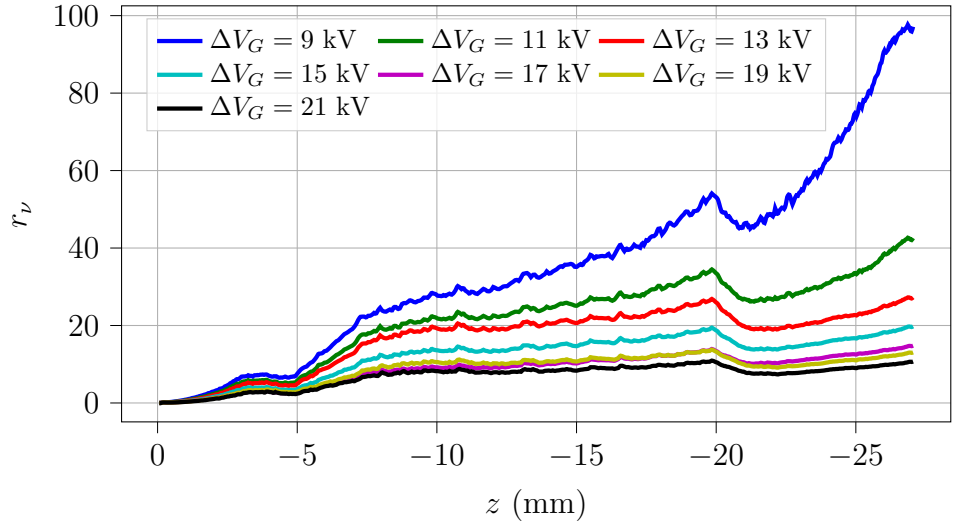

Figure 15: Turbulence intensity on symmetry axis for $\Delta V_G = 12$ kV (solid lines), $\Delta V_G = 4$ kV (dotted lines) and different values of d

The correlations between I_t and ΔV_G, and between I_t and d, are resp. presented on figs. 18 and 19. For this needle-to-ring geometry, we find that the inverse of I_t on the symmetry axis is nearly linear to ΔV_G while I_t is linear to d. These new features are in contrast to those of EAD jets on a blade-to-plane geometry [49], where the streamwise turbulence intensity approaches an asymptotic value in any case.

5.3. Characteristics of positive needle-to-ring EAD jets

Figure 20 shows the axial and radial components u_z, u_r of the EAD jet velocity $\boldsymbol{u}$ for $d = 20$ mm, $\psi = 10^{11}$ m^{-3}, $u_0 = 50$ m s^{-1} and different values of ΔV_G. As the

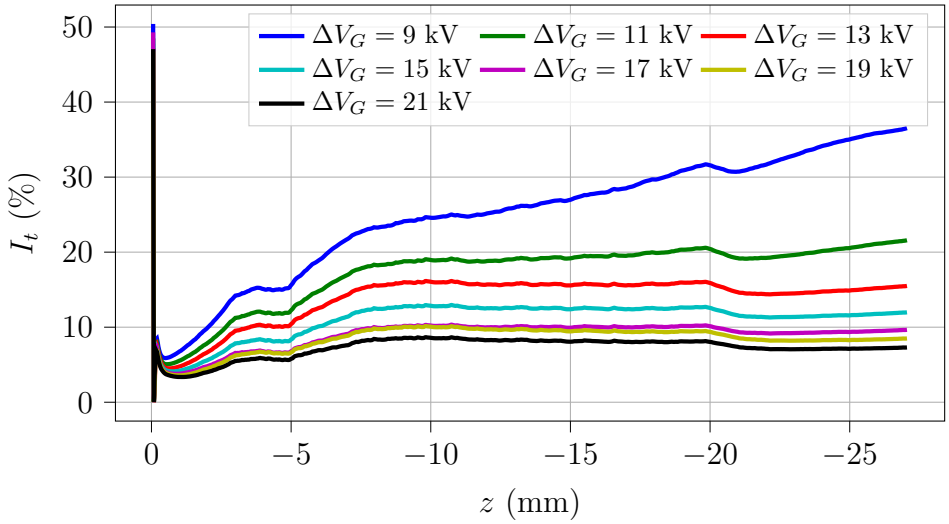

Figure 16: Turbulence intensity on symmetry axis for $d = 20$ mm and different values of ΔV_G

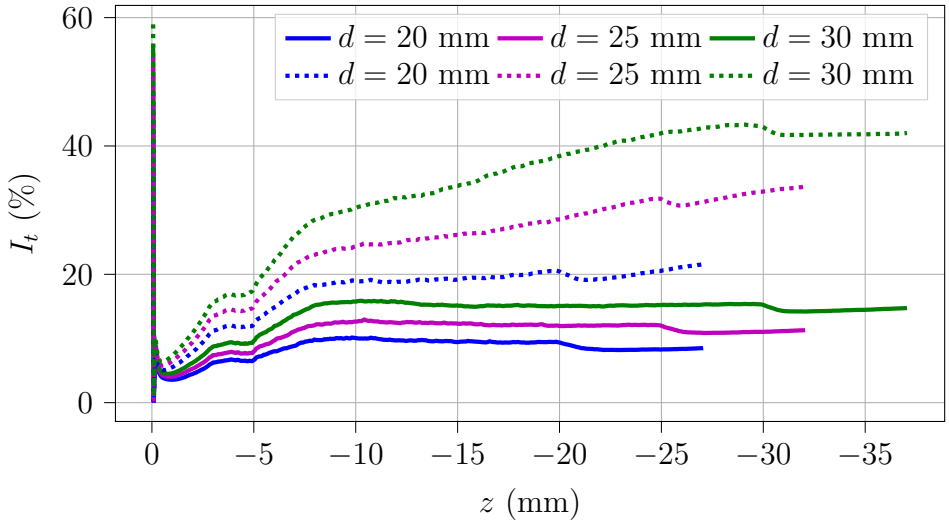

Figure 17: Turbulence intensity on symmetry axis for $\Delta V_G = 12$ kV (solid lines), $\Delta V_G = 4$ kV (dotted lines) and different values of d

EAD force increases with ΔV_G (see fig. 6), it is natural that the flow velocity also gets stronger. Furthermore, the structure of the jets, in all cases, is annular, exhibited by two panhandles in the contour maps of u_z which locate roughly at $r = 0.125$ mm, i.e. on the same location as the annular structure formed by positive ions (see section 4 and fig. 5).

Finally, the ratio $\dfrac{\max|u_r|}{\max|u_z|}$ is practically unchanged and is roughly 0.28. Even so, the annular form of the jet is accentuated with higher ΔV_G, which is possibly because

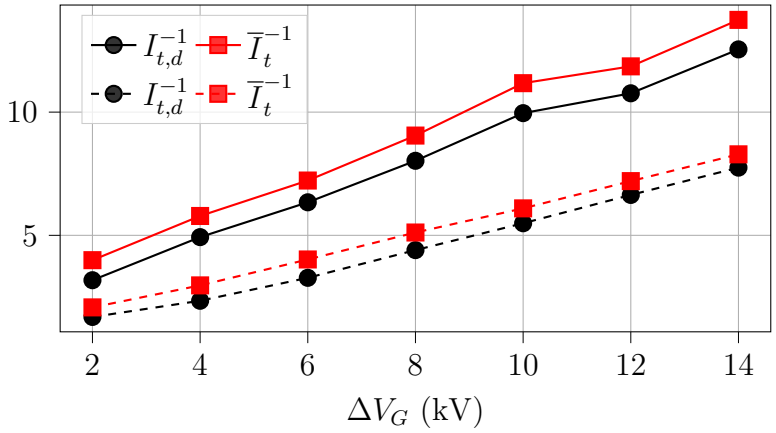

Figure 18: The inverse of turbulence intensity at $(0, -\sigma - d)$ - $I_{t,d}^{-1}$ - and the inverse of average turbulence intensity on $r = 0$ - $\overline{I}_t^{-1}$ - in function of ΔV_G, for $d = 20$ mm (solid lines) and $d = 30$ mm (dashed lines)

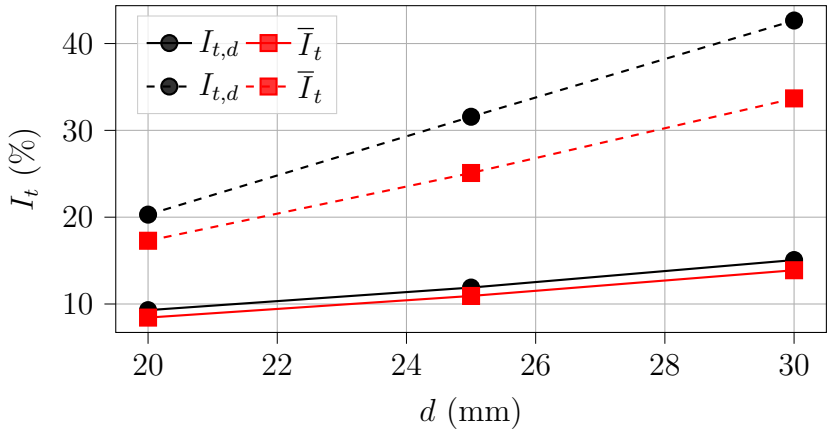

Figure 19: Turbulence intensity at $(0, -\sigma - d)$ - $I_{t,d}$ - and average turbulence intensity on $r = 0$ - $\overline{I}_t$ - in function of d, for $\Delta V_G = 12$ kV and $\Delta V_G = 4$ kV

the ratio $\dfrac{\max|F_r|}{\max|F_z|}$ is not constant but also increases with ΔV_G[+].

5.4. EAD jets and comparison with experiment data - the V-u curves

It has been experimentally and theoretically proven in [45] that the EAD jet velocity on the symmetry axis is linearly proportional to the over-voltage with the law

$$u_{|r=0} = k_{\mathrm{Vu}} \Delta V_G, \tag{11}$$

where the proportionality coefficient $k_{\mathrm{Vu}} > 0$ is tabulated for each value of d in table 5. On the same table also figure the numerical values of k_{Vu} obtained by the turbulence model

[+] $\dfrac{\max|F_r|}{\max|F_z|} = 0.58,\ 0.48,\ 0.41$ resp. for $\Delta V_G = 12,\ 8,\ 4$ kV (see fig. 6)

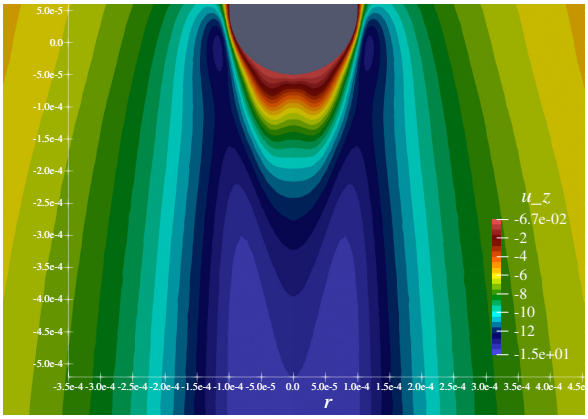

(a) u_z (m s^{-1}), $\Delta V_G = 12$ kV

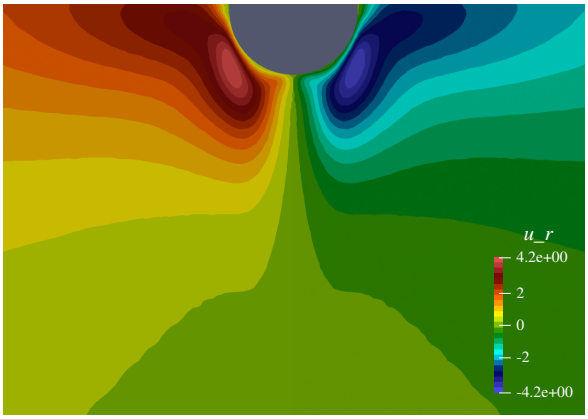

(b) u_r (m s^{-1}), $\Delta V_G = 12$ kV

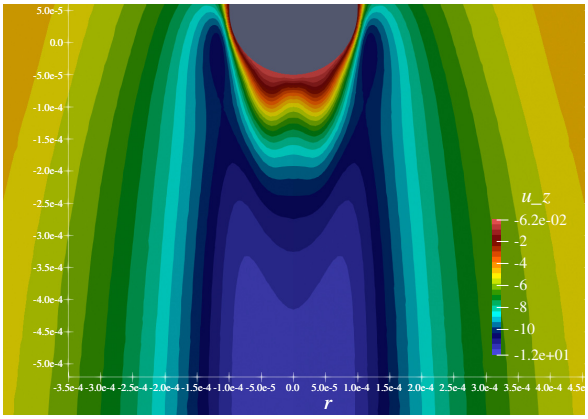

(c) u_z (m s^{-1}), $\Delta V_G = 8$ kV

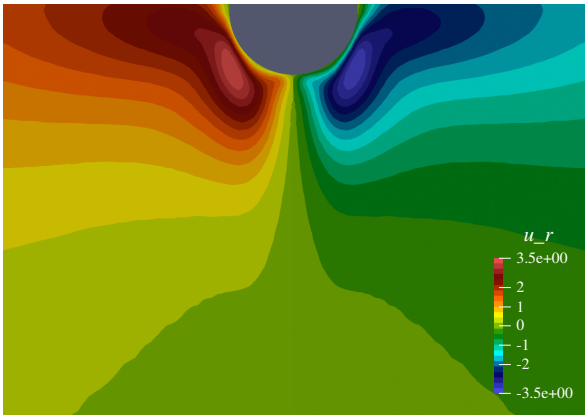

(d) u_r (m s^{-1}), $\Delta V_G = 8$ kV

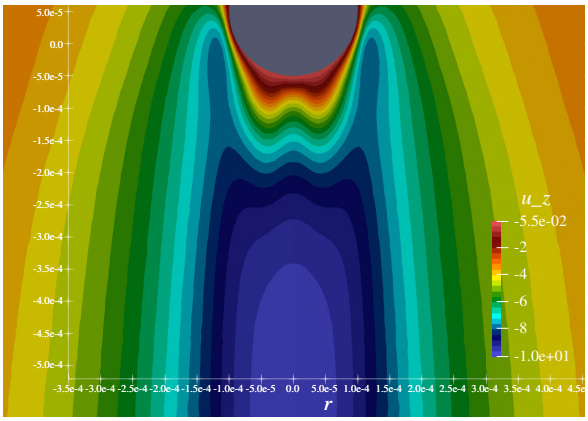

(e) u_z (m s^{-1}), $\Delta V_G = 4$ kV

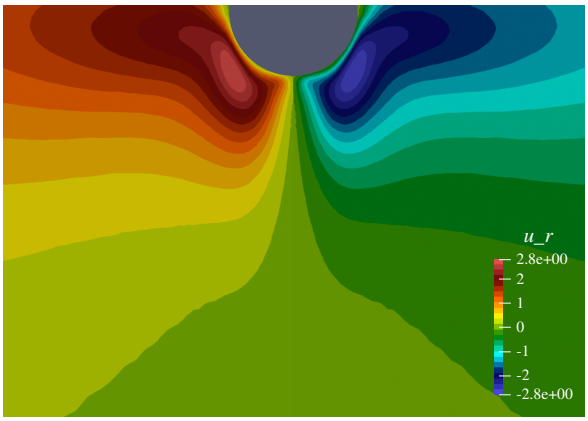

(f) u_r (m s^{-1}), $\Delta V_G = 4$ kV

Figure 20: Components of the EAD jet velocity computed with the turbulence model for $d = 20$ mm and different values of ΔV_G

	$d = 20$ mm		$d = 25$ mm		$d = 30$ mm	
	Experiment	$u = 50$ m s^{-1}	Experiment	$u = 50$ m s^{-1}	Experiment	$u = 50$ m s^{-1}
k_{Vu} (m s^{-1} kV^{-1})	0.48	0.51	0.4	0.38	0.27	0.28

Table 5: V-u characteristics of experiment data [45] and numerical solutions for different values of d

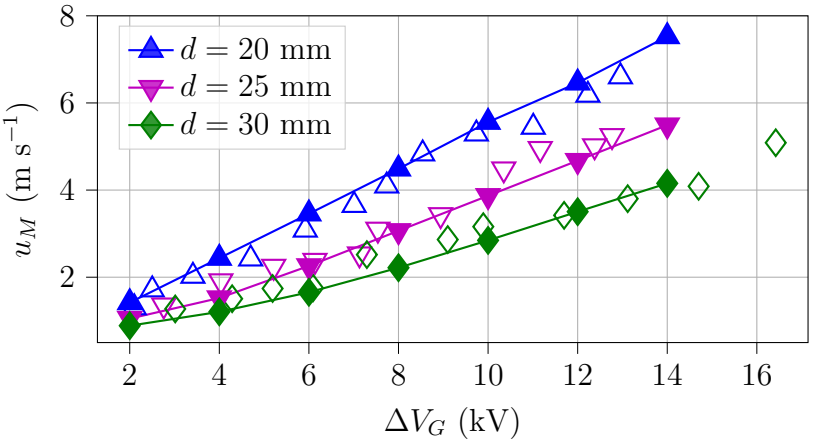

Figure 21: V-u curves of numerical solutions (filled markers) and experiment data [45] (hollow markers) for different values of d

(6)-(8) with $u_0 = 50$ m s^{-1}, where u is evaluated at the point $M = (0, -\sigma - d - h - l)$ (see fig. 1).

We then find that the numerical V-u characteristics, in contrast to the V-I characteristics, are very close to the experimentally computed slopes. In terms of magnitude, fig. 21 shows that the numerical values agree well with experiment measurements and they respect the linearity law (11). These results are quite interesting since they are achieved only once a calibration test is done for a single case (which we did in section 5.1 for $d = 20$ mm, $\psi = 10^{11}$ m^{-3} and $\Delta V_G = 12$ kV to find $u_0 = 50$ m s^{-1}). These results also confirm to a large extent, that the V-u characteristics are more reliable indicators than the V-I characteristics for assessing numerical simulations.

6. Conclusion

This work presented 2D-axisymmetric, self-consistent simulations of a needle-to-ring corona discharge, under positive applied voltages and operating in relatively dry, atmospheric-pressure air.

For the plasma discharge part, we used a set of drift-diffusion-reaction equations coupled to a Poisson equation to describe the dynamics of charged species and the evolution of the electric field. A user-defined parameter - the electron floor density ψ - was integrated into the discharge model in order to numerically control the charge density

level as well as the electric current. A robust implicit scheme was used to accelerate the calculations.

For the ionic wind part, we used the realizable k-ε equations - a RANS model - to compute the EAD jet velocity and turbulence intensity. It was necessary to adjust the inlet boundary values of k and ε in order to get the right results comparing to experiment data. By fixing the inlet turbulence intensity to 1% and the Prandtl mixing length to 5% of the cathode's (ring) inner diameter, the only remaining free parameter is the reference flow velocity u_0.

The main findings of this work are summarized as follows.

(i) The distribution of positive charges and EAD force, as well as the structure of the EAD jets had an annular form around the anode (needle). This special morphology was thought to originate from the needle-ring geometry.

(ii) For the plasma discharge simulations, $\psi = 10^{11}$ m^{-3} seemed to be the best value to match the numerical results (electric current) to the measurements in [45]. The same value of ψ was used in our previous studies [27, 41] for other geometries.

(iii) The potential-current characteristics (V-I curves) of the numerical solutions satisfied a quadratic law as predicted by theory [45]. Nevertheless, they present slight deviations from experimental data.

(iv) For the ionic wind simulations, positive-corona-induced jets were reconfirmed to be laminar-turbulent transitional flows. This conclusion was supported by two turbulence indicators: the ratio between eddy viscosity and air viscosity r_ν, and the turbulence intensity I_t. In our tests, r_ν varied between 0-200 while I_t was on the order of 10-40%.

(v) For the turbulence model, $u_0 = 50$ m s^{-1} provided good flow velocity comparing to experiment data [45], at least in the jet core region. The potential-velocity characteristics show less discrepancy in general compared to the V-I curves, and is likely a better indicator for the model validity.

(vi) Outside of the jet core region, numerous attempts were made (see also Appendix B) but could not match the experimental data in a satisfactory manner. We speculate that the experimental setup might introduce some "parasitic" effects that can not be captured by the numerical model due to lack of detailed information on the exact experimental setup.

(vii) Finally, the potential-flow velocity characteristics (V-u curves) of the numerical solutions satisfied a linear law as predicted by theory [45] and agreed well with the experiment measurements.

While the numerical and physical models used in this study surely provide a better approximation than more simplified models of corona discharges and EAD generation, the results still suggest that various tuning and model parameters need to be carefully be accounted for when interpreting the results. A detailed experimental-numerical campaign in controlled environments should be used in the future to confirm all the hypotheses

and clarify phenomena linked to both the spatiotemporal evolution of charged species and consequently EAD force production, but also the evolution of the entrained jet flow in similar configurations. Despite this fact, the simulations presented here showcase that well-adapted, self-consistent numerical tools, can be used without excessive CPU cost to parameterize, optimize and help design more efficient EAD propulsion systems.

Acknowledgments

The authors thank Dr. François Chedevergne (ONERA Toulouse) for enlightening and motivating discussions on turbulence modeling, as well as for his expert comments during the development of this work.

Appendix A. The realizable k-ε turbulence model

The coefficient $C_\nu(\boldsymbol{x})$ in eq. (8) is given as follows [50],

$$C_\nu = \frac{1}{A_0 + A_S u^* \frac{k}{\varepsilon}},$$

where

$$A_0 = 4, \quad A_S = \sqrt{6}\cos(\varphi), \quad u^* = (\mathbb{D}\bullet\mathbb{D} + \mathbb{O}\bullet\mathbb{O})^{\frac{1}{2}}$$
$$\varphi = \frac{1}{3}\cos^{-1}(\sqrt{6}W), \quad \mathbb{D} = \frac{1}{2}(\nabla\boldsymbol{u} + \nabla\boldsymbol{u}^t), \quad \mathbb{O} = \frac{1}{2}(\nabla\boldsymbol{u} - \nabla\boldsymbol{u}^t)$$
$$W = \min\left(\max\left(\frac{(\mathbb{D}\mathbb{D})\bullet\mathbb{D}}{\mathbb{D}\bullet\mathbb{D}}, -\frac{1}{\sqrt{6}}\right), \frac{1}{\sqrt{6}}\right)$$

Here, $\nabla\boldsymbol{u}^t$ is the transpose of $\nabla\boldsymbol{u}$ while $(\mathbb{M}\mathbb{M})_{i,j} = \sum_k \mathbb{M}_{i,k}\mathbb{M}_{k,j}$ and $\mathbb{M}\bullet\mathbb{M} = \sum_{i,j}\mathbb{M}_{i,j}\mathbb{M}_{i,j}$ for any square matrix $\mathbb{M}$.

Finally, the turbulence kinetic energy per unit mass $k(\boldsymbol{x})$ and the turbulence kinetic energy dissipation rate $\varepsilon(\boldsymbol{x})$ satisfy the following equations [51],

$$\begin{cases} \nabla\cdot(k\boldsymbol{u}) = \nabla\cdot\left(\left(\nu + \dfrac{\nu_t}{\sigma_k}\right)\nabla k\right) + G_k - \varepsilon, \\ \nabla\cdot(\varepsilon\boldsymbol{u}) = \nabla\cdot\left(\left(\nu + \dfrac{\nu_t}{\sigma_\varepsilon}\right)\nabla\varepsilon\right) + C_{\varepsilon,1}\varepsilon(2\mathbb{D}\bullet\mathbb{D})^{\frac{1}{2}} - C_{\varepsilon,2}\dfrac{\varepsilon^2}{k+\sqrt{\nu\varepsilon}}, \end{cases}$$

with

$$\sigma_k = 1, \quad G_k = 2\nu_t\mathbb{D}\bullet\mathbb{D},$$
$$\sigma_\varepsilon = 1.2, \quad C_{\varepsilon,1} = \max\left(0.43, \frac{\chi}{\chi+5}\right), \quad C_{\varepsilon,2} = 1.9, \quad \chi = \frac{k}{\varepsilon}(2\mathbb{D}\bullet\mathbb{D})^{\frac{1}{2}}.$$

Appendix B. EAD jets on different computation domains

This sections presents the computed EAD jets on some different meshes in an attempt to fit the numerical results to the experiment measurements outside the jet core,

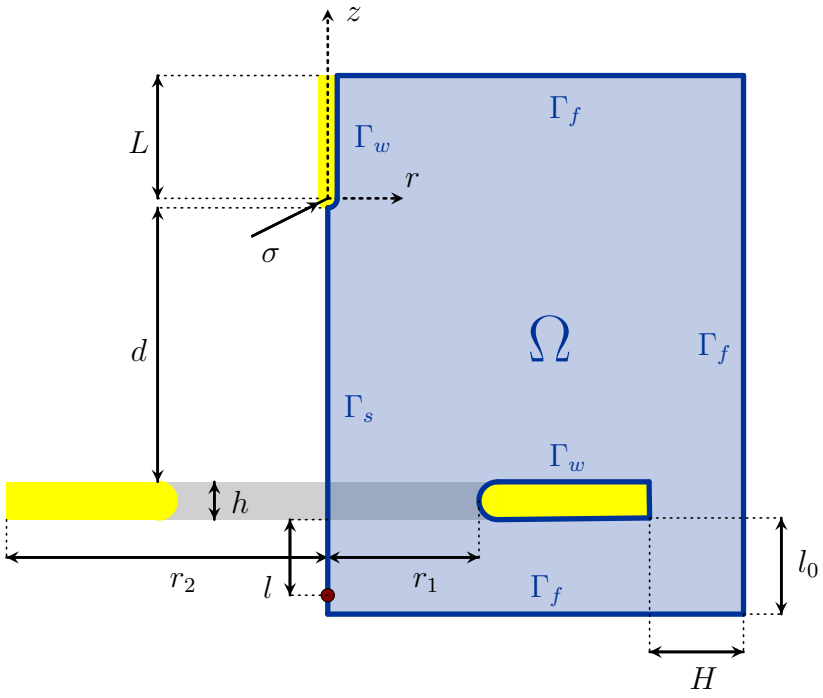

Figure B1: Sketch of the needle-to-ring actuator (not scaled to size), where the computation domain Ω, for ionic wind simulations, is colored in blue

i.e. for $r > 2$ mm (see section 5.1). Since the jet velocity in this region is practically unchanged whether the laminar model or the turbulence model is used (see again fig. 13), all the simulations in this section are obtained with the laminar model (6)-(7).

Figure B1 displays a sketch of the computation domain for the EAD jet simulations. On 2D‡, the EAD jet domain is similar to the discharge domain (fig. 1) but more extended upstream, downstream and/or away from the symmetry axis. The domain boundary is partitioned into Γ_s (symmetry axis), Γ_w (electrode surfaces) and Γ_f (free-flow boundaries). The boundary conditions are documented in table B1§‖¶.

For all the meshes considered hereafter, $\sigma = 0.1$ mm, $r_1 = 10$ mm, $r_2 = 20$ mm, $d = 20$ mm, $h = 2$ mm and $l = 5$ mm. Other geometric factors can be found in table B2.

Figure B2 shows the laminar EAD jets computed on Mesh#1, Mesh#2 and Mesh#3. In the outer region $r > 2$ mm of the jet core, we observe that the numerical flow velocity is practically the same in all the cases, and is substantially larger than the experimentally measured velocity. This discrepancy between simulations and experiments is left unexplained and we can only speculate that in the experimental domain, influence

‡ simulations with OpenFOAM actually require a 3D domain where the original 2D domain is extruded around the symmetry axis to form a wedge
§ BCs on $\boldsymbol{u}$ and p are the same for both laminar and turbulence models
‖ for k (resp. ε), `$internalField` equals to k_{in} (resp. ε_{in}) in eq. (9)
¶ we left out the top, bottom and right surfaces of the 3D domain; in the simulations, boundary conditions of OpenFOAM type `wedge` are imposed on these surfaces

	Γ_w	Γ_f
$\boldsymbol{u}$	type `noSlip`	type `pressureInletOutletVelocity`
		value `uniform (0 0 0)`
p	type `fixedFluxPressure`	type `totalPressure`
		p_0 `uniform 0`
		value `uniform 0`
k	type `kqRWallFunction`	type `inletOutlet`
	value `$internalField`	inletValue `$internalField`
		value `$internalField`
ε	type `epsilonWallFunction`	type `inletOutlet`
	value `$internalField`	inletValue `$internalField`
		value `$internalField`

Table B1: Boundary conditions (OpenFOAM [46]) for ionic wind simulations

	Mesh#1	Mesh#2	Mesh#3
l_0 (mm)	5	17.95	5
H (mm)	0	20	0
L (mm)	5	19.95	10
$\Delta x_{\min}$ (μm)	4.5	2	4

Table B2: Geometric factors for different meshes (Mesh#1 is the one used in section 5 for $d = 20$ mm)

from the surrounding environment (e.g. due to other metal surfaces that could collect charges, entrained flow confimenent etc.) played a pivotal role in the charge distribution and flow entrainment away from the jet core.

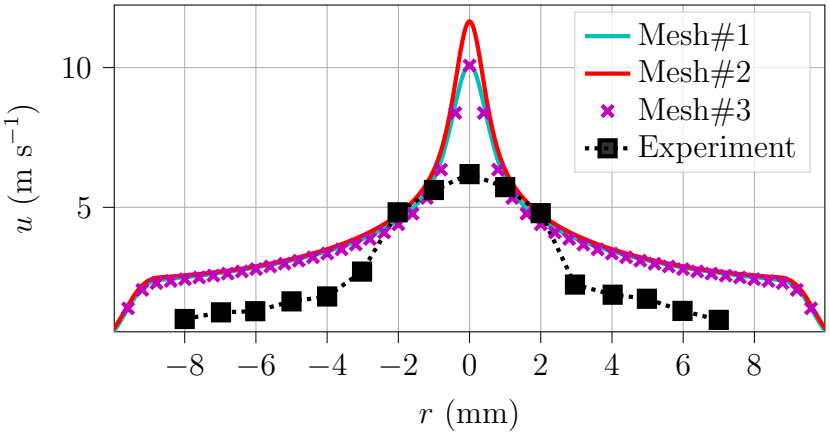

Figure B2: EAD jet velocity at $z = -27.1$ mm - or 5 mm downstream of the cathode - for $d = 20$ mm and $\Delta V_G = 12$ kV. Comparison between laminar flows obtained on different meshes and experiment data [45].

References

[1] Podliński J, Dekowski J, Mizeraczyk J, Brocilo D and Chang J S 2006 *Journal of Electrostatics* **64** 259–262

[2] Krupa A, Podliński J, Mizeraczyk J and Jaworek A 2019 *Powder Technology* **344** 475–486

[3] Huang R T, Sheu W J and Wang C C 2009 *Energy Conversion and Management* **50** 1789–1796

[4] Jewell-Larsen N, Ran H, Zhang Y, Schwiebert M, Tessera K H and Mamishev A 2009 Electrohydrodynamic (ehd) cooled laptop *2009 25th Annual IEEE Semiconductor Thermal Measurement and Management Symposium* (IEEE) pp 261–266

[5] Alamgholilou A and Esmaeilzadeh E 2012 *Experimental Thermal and Fluid Science* **38** 61–73

[6] Lai F and Lai K W 2002 *Drying technology* **20** 1393–1405

[7] Chang J S, Tsubone H, Harvel G D and Urashima K 2010 *IEEE Transactions on Industry Applications* **46** 1151–1158

[8] Dingchen L, Chuan L, Jiawei L, Wendi Y, Menghan X, Zhang M, Yong Y and Kexun Y 2022 *Plasma Science and Technology* **24** 095502

[9] Moreau E 2007 *Journal of physics D: applied physics* **40** 605

[10] Wilson J, Perkins H D and Thompson W K 2009 An investigation of ionic wind propulsion Tech. rep.

[11] Masuyama K and Barrett S R 2013 *Proceedings of the Royal Society A: Mathematical, Physical and Engineering Sciences* **469** 20120623

[12] Gilmore C K and Barrett S R 2015 *Proceedings of the Royal Society A: Mathematical, Physical and Engineering Sciences* **471** 20140912

[13] Pekker L and Young M 2011 *journal of propulsion and power* **27** 786–792

[14] Moreau E, Benard N, Alicalapa F and Douyère A 2015 *Journal of Electrostatics* **76** 194–200

[15] Granados V H, Pinheiro M J and Sá P A 2016 *Physics of Plasmas* **23**

[16] Drew D, Contreras D S and Pister K S 2017 First thrust from a microfabricated atmospheric ion engine *2017 IEEE 30th International Conference on Micro Electro Mechanical Systems (MEMS)* (IEEE) pp 346–349

[17] Xu H, He Y, Strobel K L, Gilmore C K, Kelley S P, Hennick C C, Sebastian T, Woolston M R, Perreault D J and Barrett S R 2018 *Nature* **563** 532–535

[18] Gomez-Vega N, Kambhampaty J D and Barrett S R 2022 *Journal of Physics D: Applied Physics* **55** 505202

[19] Xu H, Gomez-Vega N, Agrawal D R and Barrett S R 2019 *Journal of Physics D: Applied Physics* **53** 025202
[20] Duduta M, de Rivaz S, Clarke D R and Wood R J 2018 *Batteries & Supercaps* **1** 131–134
[21] He Y and Perreault D J 2021 *IEEE Journal of Emerging and Selected Topics in Industrial Electronics* **2** 453–463
[22] Adamiak K, Atrazhev V and Atten P 2005 *IEEE Transactions on dielectrics and electrical insulation* **12** 1015–1024
[23] Khaddour B, Atten P and Coulomb J L 2008 *Journal of Electrostatics* **66** 254–262
[24] Mantach S 2018 *Simplified Numerical Models in Simulating Corona Discharge and EHD Flows* Ph.D. thesis The University of Western Ontario (Canada)
[25] Guan Y, Vaddi R S, Aliseda A and Novosselov I 2018 *Physical Review Fluids* **3** 043701
[26] Matéo-Vélez J, Degond P, Rogier F, Séraudie A and Thivet F 2008 *Journal of Physics D: Applied Physics* **41** 035205
[27] Loehrmann A, Rivenc J, Peres G, Dufour G, Rogier F and Kourtzanidis K 2021 Numerical and experimental correlation on electro-hydro dynamic system for small aircraft propulsion *2021 AIAA/IEEE Electric Aircraft Technologies Symposium (EATS)* (IEEE) pp 1–12
[28] Picella F, Fabre D and Plouraboué F 2024 *AIAA Journal* 1–12
[29] Chen S, Nobelen J and Nijdam S 2017 *Plasma Sources Science and Technology* **26** 095005
[30] Boeuf J and Pitchford L 2005 *Journal of Applied Physics* **97**
[31] Boeuf J P, Lagmich Y, Unfer T, Callegari T and Pitchford L C 2007 *Journal of Physics D: Applied Physics* **40** 652
[32] Lagmich Y, Callegari T, Pitchford L C and Boeuf J P 2008 *Journal of Physics D: Applied Physics* **41** 095205
[33] Boeuf J, Lagmich Y and Pitchford L 2009 *Journal of applied physics* **106** 023115
[34] Kourtzanidis K, Dufour G and Rogier F 2020 *Journal of Physics D: Applied Physics* **54** 045203
[35] Kourtzanidis K, Dufour G and Rogier F 2021 *Journal of Physics D: Applied Physics* **54** 26LT01
[36] Borradaile H, Kourtzanidis K, Rogier F, Choi K S and Mao X 2021 *Journal of Physics D: Applied Physics* **54** 345202
[37] Kourtzanidis K 2023 *Plasma Sources Science and Technology* **32** 105016
[38] Dufour G and Rogier F 2015 *Aerospace Lab*
[39] Hagelaar G J M 2000 *Modeling of microdischarges for display technology* vol 109 (Technische Universiteit Eindhoven Eindhoven)
[40] Hagelaar G and Pitchford L C 2005 *Plasma sources science and technology* **14** 722
[41] Nguyen T D, Besse C and Rogier F 2023 *Computer Physics Communications* 108906
[42] Aubin J P and Cellina A 2012 *Differential inclusions: set-valued maps and viability theory* vol 264 (Springer Science & Business Media)
[43] Geuzaine C and Remacle J F 2009 *International journal for numerical methods in engineering* **79** 1309–1331
[44] Greenshields C and Weller H 2022
[45] Zhang Y, Liu L, Chen Y and Ouyang J 2015 *Journal of Electrostatics* **74** 15–20
[46] Weller H, Tabor G, Jasak H and Fureby C 1998 *Computers in physics* **12** 620–631
[47] Liang W J and Lin T 1994 *Aerosol Science and Technology* **20** 330–344
[48] Rickard M and Dunn-Rankin D 2007 *Journal of Electrostatics* **65** 646–654
[49] Yan Z, Louste C, Traoré P and Romat H 2013 *IEEE Transactions on Industry Applications* **49** 2314–2322
[50] Marzouk O and Huckaby E 2010 *Engineering Letters* **18**
[51] Shih T, Liou W, Shabbir A, Yang Z and Zhu J 1994 A new k-epsilon eddy viscosity model for high reynolds number turbulent flows: Model development and validation Tech. rep.